Imaging, Domain Writing and Spectroscopy using Scanning Probes

Ashima Arora

A dissertation submitted for the partial fulfilment of BS-MS dual degree in Science

Indian Institute of Science Education and Research, Mohali
April 2014

Certificate of Examination

This is to certify that the dissertation titled **Imaging, Domain Writing and Spectroscopy using Scanning Probes** submitted by **Ashima Arora** (Reg. No. MS09026) for the partial fulfilment of BS-MS dual degree programme of the Institute, has been examined by the thesis committee duly appointed by the Institute. The committee finds the work done by the candidate satisfactory and recommends that the report be accepted.

Dr. Sanjeev Kumar Dr. Yogesh Singh Dr. Goutam Sheet
(Supervisor)

Dated: April 25, 2014

Declaration

The work presented in this dissertation has been carried out by me under the guidance of Dr. Goutam Sheet at the Indian Institute of Science Education and Research Mohali.

This work has not been submitted in part or in full for a degree, a diploma, or a fellowship to any other university or institute. Whenever contributions of others are involved, every effort is made to indicate this clearly, with due acknowledgement of collaborative research and discussions. This thesis is a bonafide record of original work done by me and all sources listed within have been detailed in the bibliography.

Ashima Arora
(Candidate)

Dated: April 25, 2014

In my capacity as the supervisor of the candidate's project work, I certify that the above statements by the candidate are true to the best of my knowledge.

Dr. Goutam Sheet
(Supervisor)

Acknowledgements

I would like to thank Dr. Goutam Sheet, my thesis supervisor for his guidance and encouragement during the course of my project work. I am thankful to Dr. Kamal P. Singh, Dr. Santanu Pal, Dr. Samrat Mukhopadhyay, Dr. Yogesh Singh, Dr. Sanjeev Kumar , Dr. Kanishka Biswas for their help during this work.

I am indebted to all the lab members namely, Jithin B.P., Prateek Gupta, Jagmeet Singh Sekhon, Avtar Singh and Leena Agarwal for their help. I thank you all for the fun times that made the lab even a better place to work. I am thankful to Nishtha Agarwal, Monika Gupta and Dr. Pramod Kumar for their help during this work.

A special thanks to my family. Words cannot express how grateful I am to my parents for their unconditional love and support.

List of Figures

Contents

Abstract

In this thesis work, we have standardized the different operational modes of commercial atomic force microscope(AFM) including Non-contact and Contact topography, Force Mapping, Lateral Force Microscopy (LFM), Magnetic Force Microscopy, Piezoresponse Force Microscopy (PFM), Electrostatic Force Microscopy (EFM) and Conductive AFM. Using the above mentioned experimental techniques we have shown that mechanical properties like friction and adhesion is modulated in a quasi-periodic fashion in correlation with topographic modulation in certain transparent insect wings. The natural motivation for such modulation is not understood and that might be an important open problem in biology. The surface of these wings have self-cleaning and anti-wetting properties. This work is significant in the context that it has meritorious applications in fabrication of artificial surfaces having such properties.

We have used Piezoresponse Force Microscopy to show that electrically active domains can be written and erased on single crystals of $SrTiO_3$ at remarkably high temperatures up to 440K. Observation of hysteretic phase switching indicates that $SrTiO_3$ might have a high temperature ferroelectric phase. Since the surface of $SrTiO_3$ is itself electrically active, its usage as a substrate and hetero-structures such as $LaAlO_3$/$SrTiO_3$ should be revisited.

We also investigate the ferroelectric behaviour of a recently discovered thermoelectric semiconductor $AgSbSe_2$ and we infer that it possesses nanometer scale ferroelectric domains that could potentially scatter mid-wavelength phonons and reduce thermal conductivity thereby enhancing the thermoelectric figure of merit (zT).

Chapter 1

Introduction

1.1 Scanning Probe Microscopy

Scanning Probe Microscopy (SPM) is one of the most powerful imaging techniques that employ a mechanical probe to investigate the surface topography and local properties of samples. With the ability to operate over micron to nano-meter length scales, SPM provides an opportunity to study a variety of systems with atomic resolution. The first member of the SPM family was the Scanning Tunneling Microscope which was invented by Gerd Binnig and Heinrich Rohrer in 1981.[1] Their contribution was highly acknowledged and they were awarded Nobel Price in Physics in 1986. SPM finds its applications in wide variety of areas such as physics, material science, biology, chemistry, etc. With a rapid increase in scientific research and technology, other scanning probe microscopes like the Atomic Force Microscope, Magnetic Force Microscope, Near Field Scanning Optical Microscope etc. were developed and are now being widely used in different fields. [2, 3]

1.1.1 Basic Principle of SPM

The surface of the specimen is investigated with the help of a sharp tip whose apex is of the order of few nanometers. A topographic map of the sample can be constructed by exploiting the interactions between the tip and the sample. The type of interaction depends upon the kind of microscope and the property to be studied. The typical distance between the tip and the sample is about 1-2 nm. The interaction between the tip and the sample is quantified in terms of a parameter T. As the tip scans over the sample, the value of this parameter changes due to interactions between the tip and the sample. The feedback loop tries to maintain this parameter at some specific preset value T' by adjusting the tip-sample distance, thereby

making the error in equation 1 zero.

$$Error = T - T' \tag{1.1}$$

By analyzing the signal that the feedback loop sends to change the tip-sample distance in real time, a topographic image or the image constituting the information about the properties of the sample is constructed. Figure 1.1 shows a schematic diagram of the basic working principle of a scanning probe microscope.

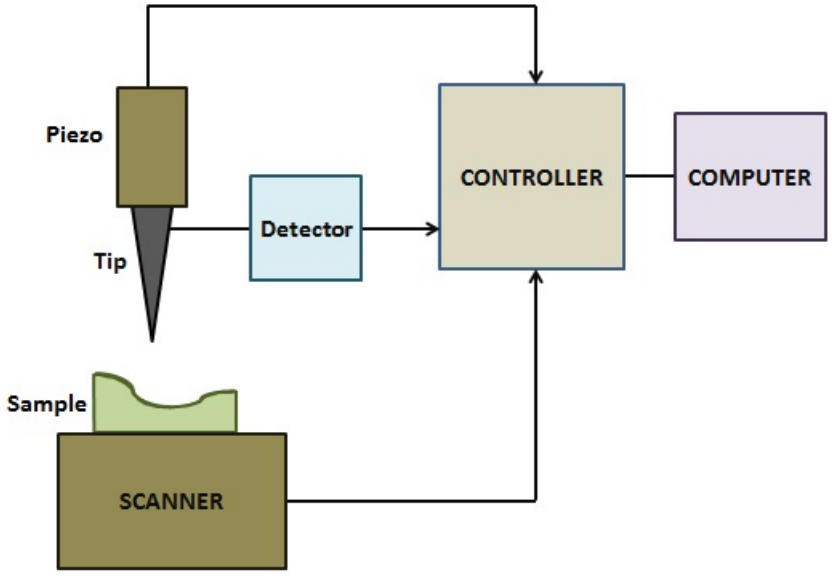

Figure 1.1: A schematic diagram showing the basic working principle of a Scanning Probe Microscope

1.1.2 Scanning Tunneling Microscope

The first member of SPM family, the Scanning Tunneling Microscope utilizes tunneling current between a conducting tip and sample to probe the properties of a sample [4, 5]. Figure 1.2 shows a schematic diagram of a general Scanning Tunneling Microscope. The tip is mounted on a scanner which allows three-dimensional positioning in the x, y, and z directions with subatomic precision using piezo-tubes. The tip-sample distance is reduced to few Angstroms. This creates a tunneling barrier whose strength depends on the distance between the tip and the sample. In this tunneling regime,a bias voltage is necessary for the flow of tunneling current between the tip and the sample. The tunneling current has an exponential dependence and is very sensitive to the tip-sample distance.

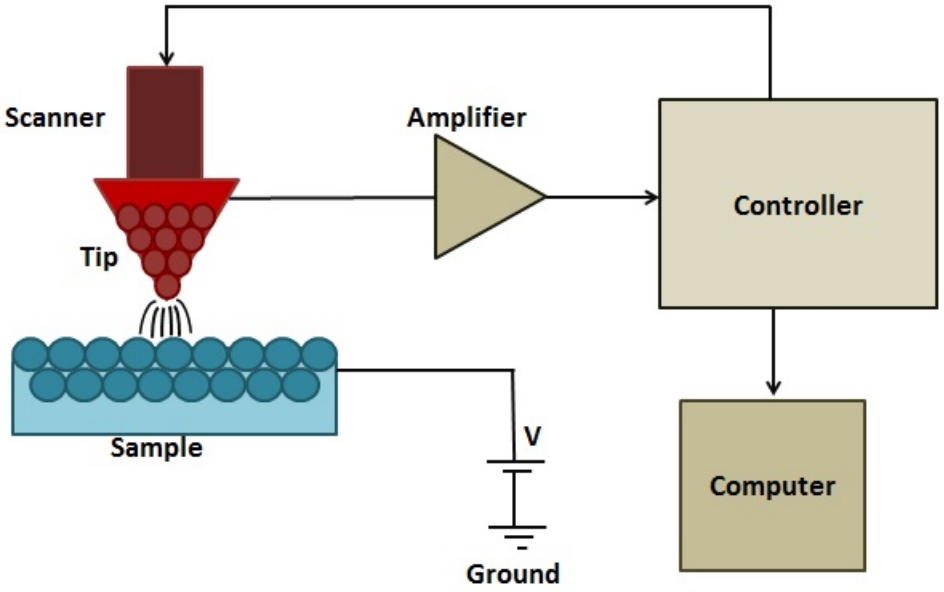

Figure 1.2: A schematic diagram of Scanning Tunneling Microscope

The most widely used convention of the polarity of bias voltage is that the tip is virtually grounded. The bias voltage V is provided to the sample. If $V > 0$, the electrons tunnel from the occupied states of the tip into the empty states of the sample. If $V < 0$, the electrons tunnel from the occupied states of the sample into the empty states of the tip. While scanning in the constant current mode, the feedback loop maintains a constant value of this tunneling current by modulating z profile with the help of the piezo. By recording the voltage applied to the z-piezo and the x-y motion of the tip, a three dimensional image of the topography of the sample's surface is obtained.

For scanning atomically smooth surfaces, constant height mode is used in which the height of the tip above the sample is fixed. This is carried out either by turning off the feedback loop or by scanning at high speeds faster than the reaction time of the feedback system.For achievement of atomic resolution, it is necessary that an atom protrudes out from the tip and reaches to the sample to a distance which is comparable to the dimensions of lattice. This is done by sharpening the tip by chemical etching or mechanical grinding. The other necessary condition is that the system should be free of vibrations. This condition is met by establishing a proper vibration isolation. [6, 7]

Despite the vast success of STM, it has a drawback that it can only probe conducting materials as it only uses tunneling current as a feedback parameter. Soon it was speculated that

at very small tip-sample distances, inter-atomic forces were significant enough to be used in a new member of SPM, Atomic Force Microscope.

1.1.3 Atomic Force Microscope

Atomic Force Microscope was first introduced in 1986 by Gerd Binnig, Calvin F. Quate and Christopher Herber.[2] The working principal of an AFM is similar to that of STM but the tip is replaced by an elastic cantilever with a sharp tip as a probe which interacts with the sample and probes the surface's properties. While STM can only probe conducting materials, AFM provides freedom to image all kind of materials regardless of their conductivity. This technique has undergone major developments since its inception and has now become an essential tool for imaging the topography and properties of samples.[8]

The interactive forces felt by the AFM tip are a combination of chemical interaction, electrostatic forces, magnetic forces, meniscus forces, vanderwal forces, etc. The vanderwal forces can be approximated by Lennard-Jones potential. With this potential, one can estimate the interaction force between tip and the sample.

$$U_{LD}(r) = U_o\{-2(\frac{r_o}{r})^6 + (\frac{r_o}{r})^{12}\} \tag{1.2}$$

Components of AFM: MFP-3D

- **Piezo Actuators and Scanners** Piezoelectric effect is the property of certain materials to generate mechanical oscillations in response to an electric voltage. This property of piezo-electricity is exploited for the precise movement of tip at nanoscale. Piezos in AFM's are widely used for scanning. The piezo moves in a specific direction (expands or contracts) depending upon the voltage applied (positive or negative).The x-y motion of the sample is controlled by the piezos in the scanner and the z-motion of the tip is controlled by the piezo stack above the cantilever. The range of scanning area in AFM's is limited to few tens of microns. This is due to the nonlinear and hysteretic behavior of displacement of piezo with applied voltage. At high voltages problems like hysteresis and piezo creeps become severe. Thus the accuracy of the displacement of the piezos' is limited to few microns.

- **Tip** The tip is the main working part of the AFM which actually interacts with the sample. It is a sharp micro-fabricated tip mounted at one end of an elastic cantilever.It

is typically made up of Silicon or Silicon Nitride with a coating depending upon the choice of experiment. [9, 10] The radius of curvature of the tip's apex is of the order of $5 - 50nm$ which limits the lateral resolution. The interactive force F between the tip and sample can given by Hook's Law.

$$F = k\Delta x \tag{1.3}$$

where k is elastic constant and the interactions between tip and sample are measured by the displacement of the cantilever Δ x.

- **Laser Based Detection** Optical techniques are used to measure the motion of the cantilever as it interacts with the sample and is effected by various kinds of forces. A laser of wavelength $860nm$ is collimated and is focused on the tip using a lens. The beam reflects from the tip and is recollimated using a lens and finally reflects by a mirror reaching a segmented photo-diode. The bending of the cantilever can be detected optically as the laser spot moves up and down on the photo-diode itself. The position of the laser on the photo-diode is determined by the angle of the deflected cantilever. A small change in the angle leads to an amplified movement of laser spot on the photo-diode. Thus, photo-diode does not needs nano-scale precision to detect the motion of the cantilever.

- **Deflection and Photo-diode** The measurement of the cantilever's displacement has to be accurate in order to achieve atomic resolution. The cantilever may be deflected vertically or laterally which is detected optically using a segmented photo-diode having four quadrants as shown in Figure 1.3.

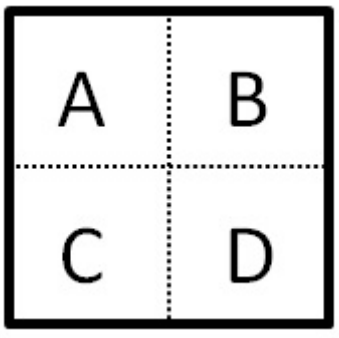

Figure 1.3: Four segmented photo-diode.

The laser spot after reflecting from the tip falls on this segmented photo-diode. A voltage is generated for each quadrant depending on the amount of the light falling on the corresponding segment. The vertical deflection is defined as the difference between the voltage generated in upper two and lower two quadrants whereas the lateral deflection is the difference between voltages generated in left and right quadrants. Figure 1.4 shows the possible position of the laser spot on the photo-diode.

$$Vertical\ Deflection = V_{top} - V_{bottom} = (V_A + V_B) - (V_C + V_D) \tag{1.4}$$

$$Lateral\ Deflection = V_{left} - V_{right} = (V_A + V_C) - (V_B + V_D) \tag{1.5}$$

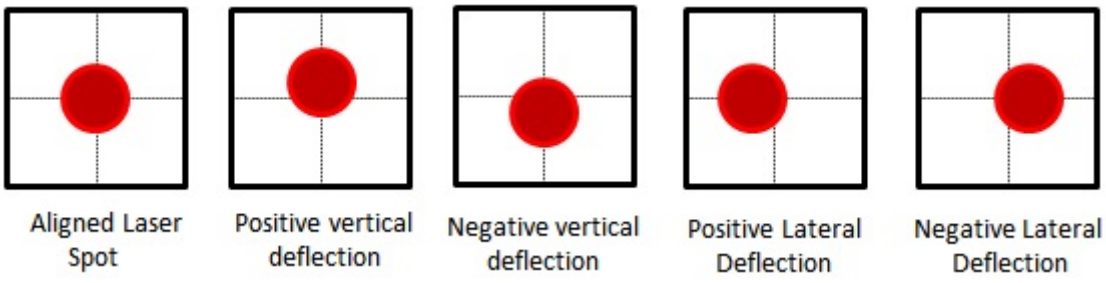

Figure 1.4: Position of laser spot in different deflections of the cantilever.

1.1.4 Operational Modes of AFM

- **Non-Contact Mode** The non-contact mode uses amplitude of oscillation of the cantilever as a feedback parameter. The shake piezo on the cantilever drives the cantilever at its resonant frequency with certain amplitude. The dynamic motion of a cantilever can be mimicked by a mechanically driven damped oscillator. The cantilever is driven by piezo with an external periodic force $F_{drive} = kA_{drive}\cos\omega t$. The simple harmonic oscillator can thus be described by a second order differential equation.

$$m\frac{d^2z}{dt^2} = F_{drive} - b\frac{dz}{dt} - kz \tag{1.6}$$

where m is cantilever's mass, b is damping coefficient and z is vertical displacement of the cantilever. On solving,

$$A = \frac{A_{drive}\omega_\circ^2}{\sqrt{(\omega_{circ}^2 - \omega^2)^2 + (\frac{\omega\omega_\circ}{Q^2})}} \tag{1.7}$$

where ω is the instantaneous frequency, $\omega_\circ$ is the resonant frequency of the cantilever and Q is the quality factor which describes energy losses in a system is given by

$$Q = \frac{k}{\omega_\circ b} = \frac{\pi\tau}{T} \tag{1.8}$$

At resonance ($\omega = \omega_\circ$), the cantilever naturally oscillates with a greater amplitude as compared to any other frequency. As the distance between the cantilever and the sample is reduced, the amplitude of oscillation of the cantilever is damped due to inter-atomic forces between the tip and the sample as shown in Figure 1.5.

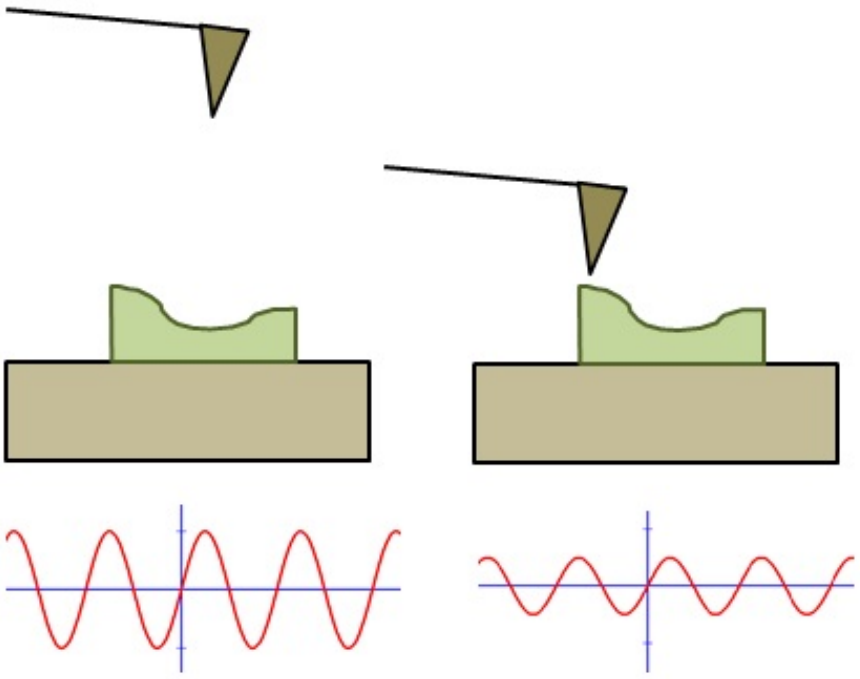

Figure 1.5: Damping of the amplitude of oscillation of the cantilever due to interactive forces between tip and the sample.

This change in amplitude is detected optically with the help of the laser and the photo-diode. As the tip oscillates, the laser spot also oscillates in phase on the photo-diode. Any perturbation in the cantilever's oscillation is thus recorded by the photo-diode. The user sets a specific value(called the 'set point') of this amplitude which has to be maintained throughout the scan with the help of z-piezo feedback loop. Thus, the feedback loop minimizes the error signal between the set point amplitude and the instantaneous amplitude (equation 1). This is carried out by giving the appropriate voltage to the z-piezo to move up or down to maintain the amplitude of the oscillation at the set point value. The contour of the sample's surface is traced by the the z-motion of the cantilever controlled by the z-piezo as shown in Figure 1.6 .[11]

Suppose there is a pit on the sample. As the tip moves past that pit, the amplitude becomes greater than the set-point as the distance between the tip and the sample is suddenly decreased. The feedback loop will increase the z-voltage supplied to the piezo making the amplitude equal to the set point value by bringing the tip closer to the sample. Similarly, if there is a height feature on the sample, the amplitude will become smaller while crossing that height feature, the feedback loop will decrease the z-voltage given to the z-piezo which will again make the amplitude equal to the set point value by retracting the tip backwards.

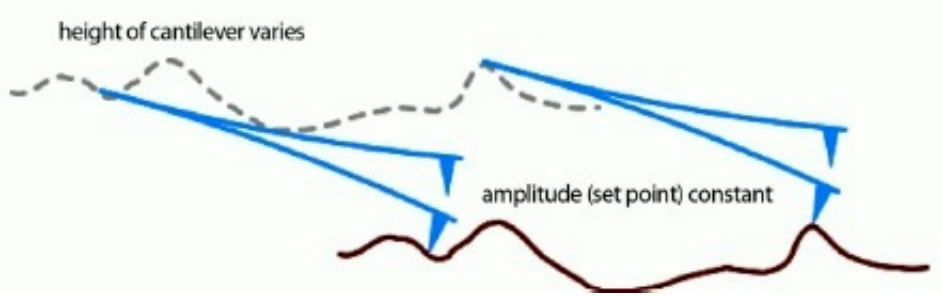

Figure 1.6: Feedback in the Non-contact Mode tracing the contour of the sample's surface.

- **Contact Mode** The contact mode uses deflection of the cantilever as a feedback parameter. A constant contact to the sample's surface is maintained throughout the scan. A contact implies that the distance between the tip and the sample is such that the inter-atomic forces between them are repulsive in nature (as shown in Figure 1.7).

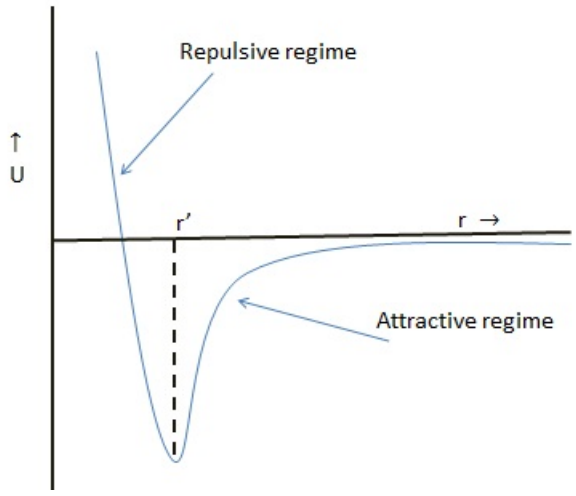

Figure 1.7: Potential versus distance showing repulsive and attractive regime.

When the tip is in contact with the sample, the cantilever bends due to repulsive force between the tip and the sample. This bending of cantilever which is termed as deflection is the angle of the cantilever and is detected optically through the photo-diode. The bending of the cantilever and the corresponding positive vertical deflection is shown in Figure 1.8.

While scanning in contact mode, the force between the tip and sample changes due to which the angle of the cantilever changes. The user chooses a particular value for deflection set point (and hence a particular value for force). The height of the cantilever is controlled by the z-piezo. As the tip scans over the sample, the z-piezo adjusts the height of the cantilever as much as needed to maintain a constant deflection set point. The z-piezo thus traces the contour of the sample's surface and maintains a constant height difference between the back end of the cantilever and the point of sample in contact with the tip throughout the scan.

Imaging in contact mode is carried out by direct mechanical contact of the tip and sample. This may damage the sample's surface or may lead to tip degradation. Due to these reasons, contact mode is not suitable for soft and biological materials.

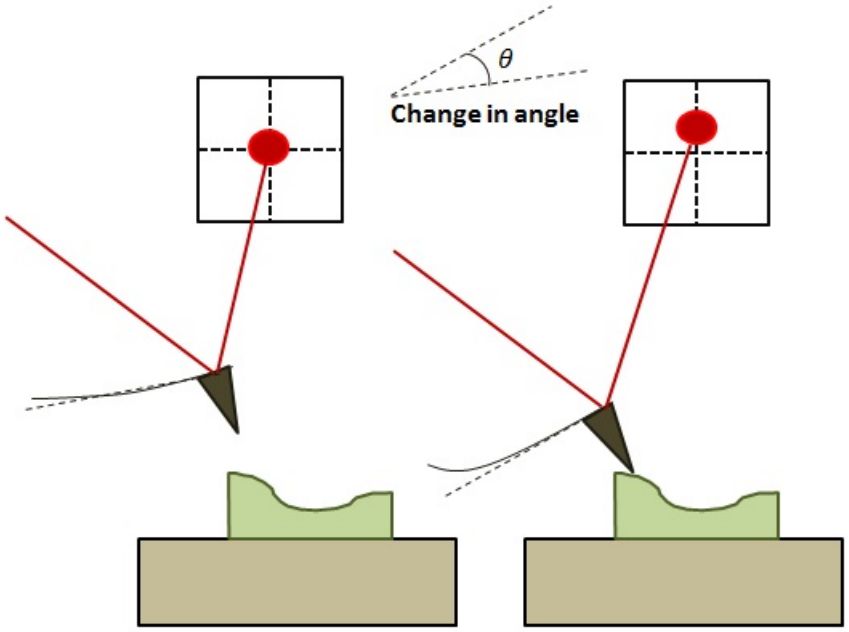

Figure 1.8: The cantilever is deflected in vertical direction which is detected through the photo-diode. The vertical deflection is basically change in the angle of the cantilever.

Chapter 2

Members of SPM

Ever since the inception of AFM, different operational modes have been developed which can probe electric, magnetic , mechanical, etc properties of samples. Some of the modes which have been used in the experiments have been described in further sections.

2.1 Lateral Force Microscopy

The ability of AFM to probe the local properties of a sample at such high resolutions has made it an important tool in the emerging field of nanotribology which is the study of atomic scale interactions between surfaces in relative motion.[12] The properties such as friction, adhesion can be easily probed with the help of Lateral Force Microscopy. Lateral Force Microscopy is carried out in contact mode and is capable of measuring lateral forces between the tip and the sample. The feedback parameter in this mode is lateral deflection. As the tip scans in contact mode, it rubs against the surface, and the friction leads to a lateral deflection of the cantilever which is measured optically. The lateral deflection of the cantilever is schematically described in Figure 2.1(a). Figure 2.1(b) shows a hypothetical surface with different topographic features having different coefficients of friction and the corresponding lateral deflections. The spikes in the lateral scan lines are seen due to a sudden rise or a sudden fall in the topography. However, if there is a sudden rise(fall) in topography and the corresponding friction also rises(falls) leading to an increase(decrease) in lateral deflection, such spikes will not appear. Therefore, the friction data measured during a single scan direction is always influenced by the topography. In our measurements we eliminate this cross-talk by recording the lateral deflection during forward (trace) and reverse (retrace) scans and then calculating the difference. The lateral retrace deflection is opposite in sign to the lateral trace deflection. Therefore, only the deflection due to friction

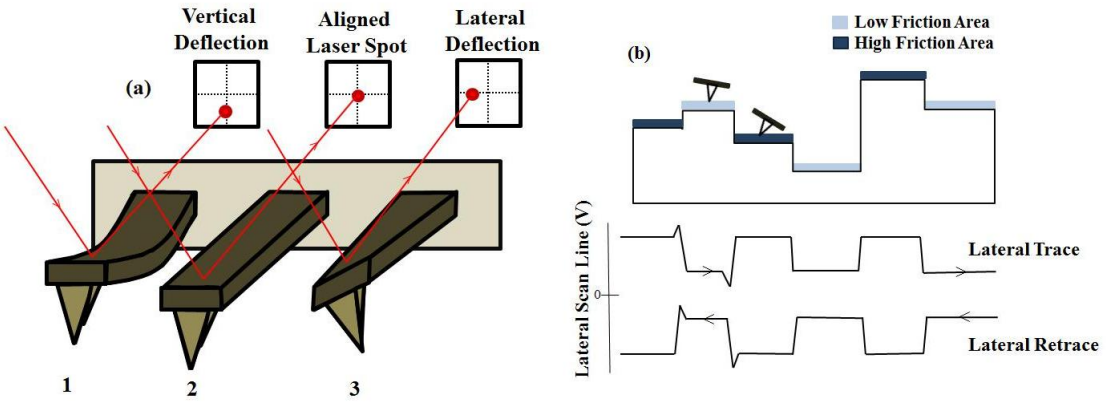

Figure 2.1: Schematic description of (a) the vertical and lateral cantilever deflection on the four-quadrant photo-detector. (b) Frictional force measurement protocol.

is retained after subtracting the two signals. The frictional data thus obtained is plotted as a function of the position of the tip on the surface in order to construct the frictional force image.

2.2 Piezoresponse Force Microscopy

PFM is known to investigate the electro-mechanical and ferroelectric properties of samples. An oscillating electric voltage is applied to a conductive tip which is in contact with the sample. The sample locally oscillates in response to this external voltage applied due to piezoelectric effect as shown in Figure 2.2. Since the tip is in contact with the sample, the mechanical oscillations thus produced are transferred to the tip. The oscillating vertical deflections of the tip are measured optically using the photo-diode.

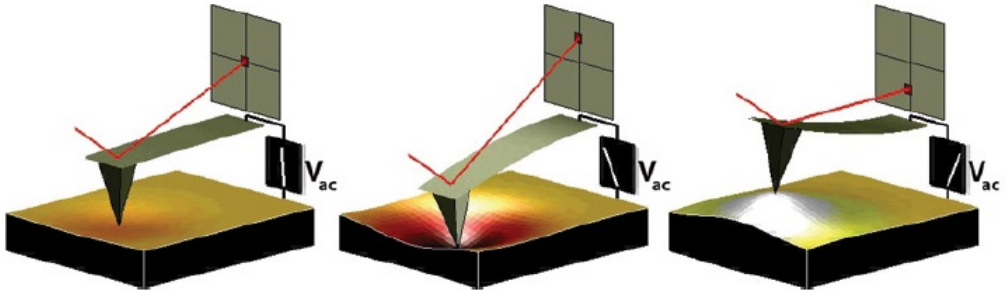

Figure 2.2: Schematic diagram showing local expansion (right), local contraction (middle) and normal state (left) in response to positive, negative and zero voltage applied respectively.

The phase of the resultant electro-mechanical response yields information about the distribution of polarization direction in the sample. Suppose the direction of polarization below the tip is upwards, then the application of positive voltage will result in local expansion of the point on the sample underneath the tip. This expansion is in phase with the voltage applied to the tip. If the direction of polarization below the tip is downwards, then a positive voltage will result in local contraction and this contraction would be out of phase with the applied voltage. As the tip crosses a domain wall with different polarization directions on its sides, a change of phase would take place as shown in Figure 2.3. Whenever the tip crosses a domain wall, it would reflected in the phase and thus a domain wall distribution in the sample is obtained.[13, 14]

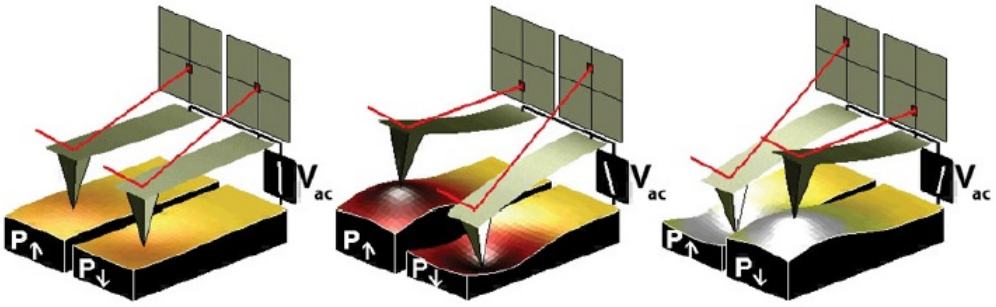

Figure 2.3: Schematic diagram showing response of the tip as it crosses a domain wall.

Piezoelectric effect produces mechanical oscillations in a sample in response to an external electric voltage. This effect is quantified by piezoelectric strain constant which is a rank-3-tensor whose d_{33} component can be measured by PFM. [15] This component is responsible for the vertical deflection of the cantilever. The voltage applied to the tip is of the form

$$V_{tip} = V_{dc} + V_{ac} \cos \omega t \tag{2.1}$$

which results in the local mechanical oscillation of the sample leading to the vertical motion of the cantilever of the form

$$z = d_{33} V_{dc} + d_{33} V_{ac} \cos(\omega t + \theta) \tag{2.2}$$

The measured PFM signal is given by

$$A = d_{33} V_{ac} Q \tag{2.3}$$

where d_{33} depends upon the materials' piezoelectric response, V_{ac} is the oscillating voltage to the tip and Q is the quality factor.

High voltage V_{ac} is avoided as it can damage the sample's surface and can also bring a change in the inherent polarization of the sample. Thus the solution to improve the piezo signal is to increase the quality factor of the cantilever. By driving the voltage at contact resonant frequency the piezoresponse signal can be boosted. The cantilever is in contact with the sample and its contact resonant frequency depends upon the tip-sample contact's stiffness. As the tip scans over a sample, the contact resonant frequency changes. This might also lead to topographic cross talk. A great way to improve the strength of the signal is to adjust the drive frequency at contact resonant frequency while scanning. To chase the resonant frequency while scanning, a new method called Dual Amplitude Resonance Tracking PFM has been developed.

2.2.1 Dual Amplitude Resonance Tracking (DART) PFM

DART, uses two lock-in amplifiers to supply voltage to the cantilever at two different frequencies. [16] Figure 2.4 shows a schematic diagram showing the working principal of DART mode PFM. An oscillating voltage supplied to the tip is a combination of voltages at two frequencies, one above the resonant frequency and one below the resonant frequency. The resultant deflection of the cantilever is sent back to the lock-in amplifiers. The change in the amplitudes at the two frequencies is measured and the contact resonant frequency is tracked by using the difference in the measured amplitudes of the cantilever ($A_1 - A_2$) as a feedback parameter.

2.2.2 Switching Spectroscopy

The piezoresponse is probed by applying an ac voltage V_{ac} between the tip and the sample which is directly connected to the ground of the voltage source. The frequency of this ac voltage is the tip-sample contact resonance frequency. For PFM spectroscopy, the ac voltage $V_{ac} = V_{ac} cos\omega t$ is mixed with a dc voltage (V_{dc}) and the sum $V = V_{dc} + V_{ac} cos\omega t$ is applied between the tip and the sample in a waveform as shown in the Figure 2.5. The area

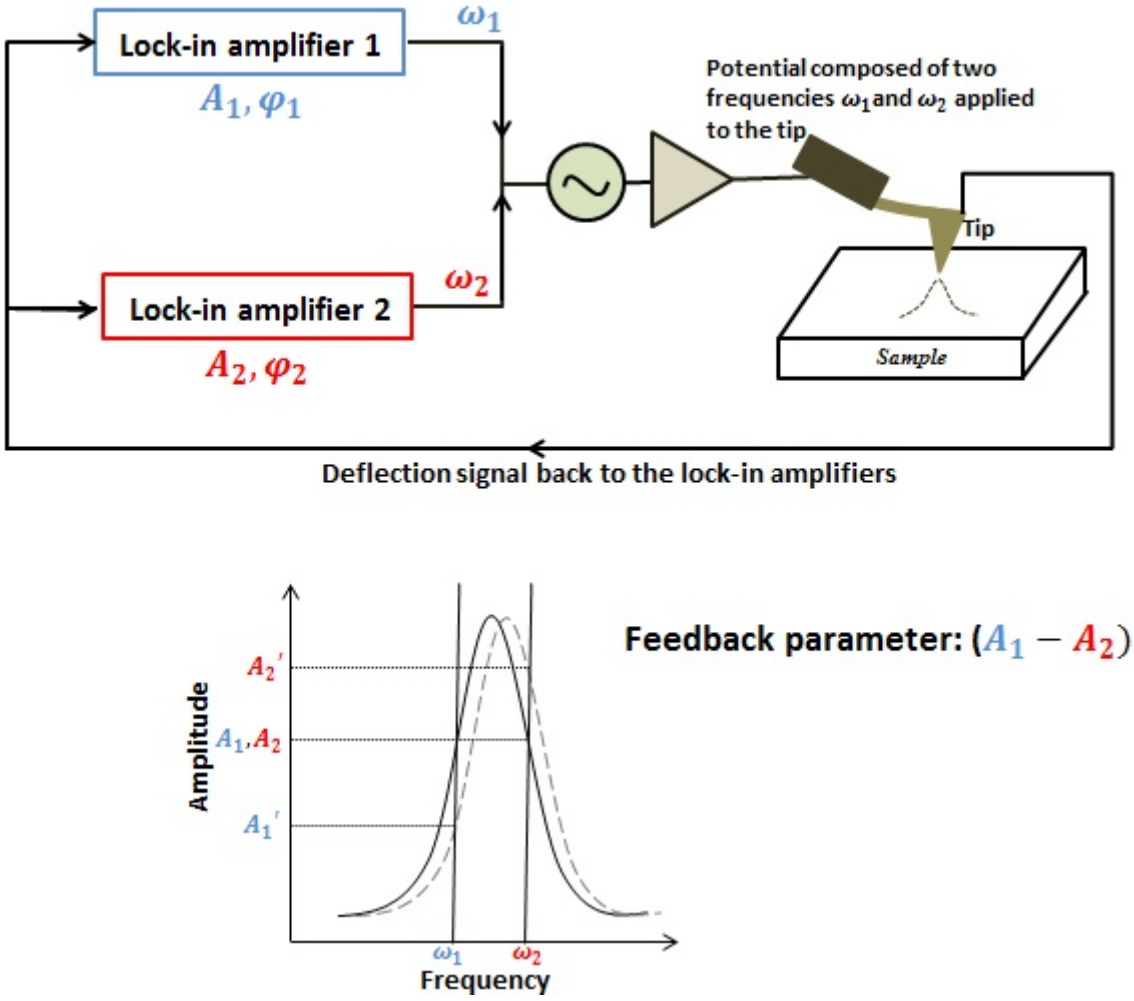

Figure 2.4: Schematic description of DART PFM

underneath the tip will be deformed due to the application of the electric field if it's piezoelectric. Since the applied field has a periodic component, the amplitude of deformation can be written as $A = A_\circ + Acos(\omega t + \phi)$, where ϕ is the phase difference between the applied field and the amplitude response. ϕ gives information about the electric polarization direction below the tip. V_{dc} switches the polarization direction in the region underneath the tip . This is expected to give rise to a 180° shift in ϕ as V_{dc} passes through $V_{dc} = 0$. In general, for ferroelectric switching, the phase ϕ switches hysteretically.

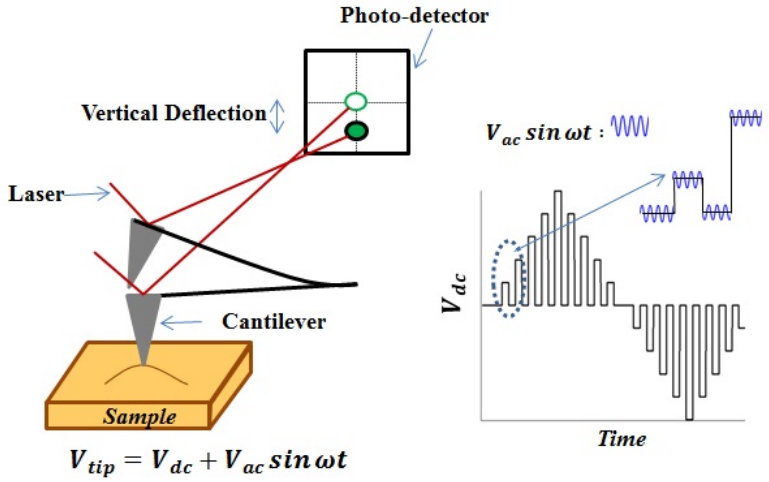

Figure 2.5: Switching spectroscopy PFM schematic diagram

2.3 Electrostatic Force Microscopy

Electrostatic Force Microscopy probes the electrostatic force which arises due to attraction or repulsion from surface charge. The cantilever is made to oscillate at its resonant frequency (non-contact mode) while a dc voltage is applied between the tip and the sample. It works on the principle that electrostatic force between the tip and the sample cause a shift in the phase. The tip-sample interaction is treated as a capacitor whose energy is given by $E = \frac{1}{2}CV^2$.[17] The force on the cantilever by electrostatic field would be obtained by differentiating this energy with respect to the z distance which is

$$F = \frac{dU}{dz} = \frac{1}{2}\frac{dC}{dz}(V_{tip} - V_{sample})^2 \tag{2.4}$$

This force depends upon the applied dc voltage and the capacitance. Capacitance is a function of tip geometry, conductivity, dielectric constant,etc. The regions having no surface charge would thus have a different $\frac{dC}{dz}$ as compared the regions having surface charge. Thus the electric field of the charges will create a different force gradient which would be reflected in the phase shift between the drive and the response of the cantilever. Nap mode is used to decouple the electric field from the topography in which two scans are performed. In the first scan, the usual topography is taken and remembered followed by a second nap scan in which the cantilever is lifted up by a constant height. This is carried out by raising the tip point by point as shown in the Figure 2.6. The force in the vertical direction varies with z distance which is recorded as a function of x-y distance. The changes in the phase

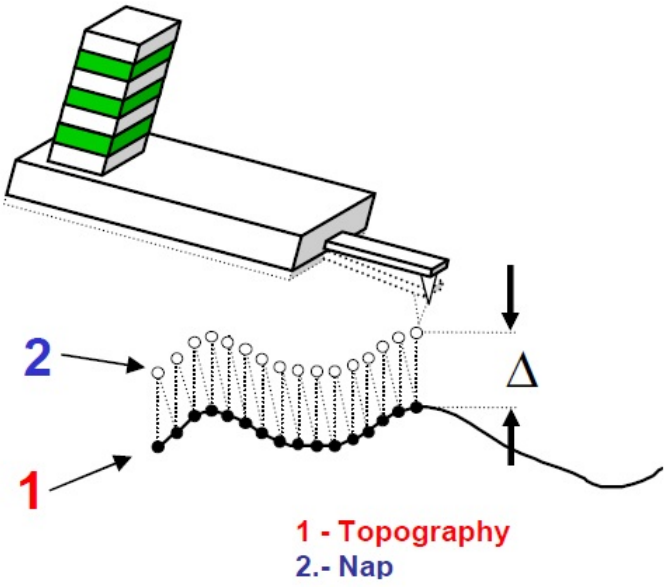

Figure 2.6: Nap mode in EFM showing two passes:Topography and Nap.

shift with x-y position provides the information about the distribution of surface charges on the sample.

Chapter 3

Nanoscale architecture: Drosophila Melanogaster

The ability of tiny insects to survive in extreme environmental conditions is remarkable. To maintain adequate mobility during rain and storm, insects have natural engineering on the surface of their wings. They are known to possess hydrophobic and self-cleaning properties which are result of superior micro and nano-structuring. The architecture of these insects' wings is expected to be used in manufacture of bio mimetic synthetic surfaces resistant to dust and water. In the past, various insects were studied and topographic micro-structures on the wing's surface were probed using various imaging and characterization techniques. With the help of high resolution Atomic Force Microscopy, it is now possible to study the topography of insects wings in much greater detail. One of the most extensively studied organisms is Drosophila Melanogaster and is a model system because of its relatively short lifetime, sequenced genome and the presence of a vast variety of mutants.[18] We have studied Drosophila Melanogasters wing to study its fascinating micro-structures and nano-structural diversity that gives rise to its extraordinary water and dust resistant properties.

The wing of a female wildtype Drosophila Melanogaster was loaded flat on a glass slide and was fixed with scotch tape at its edges. This exposed a small and flat region (away from the veins) of the wing on which AFM measurements were carried out.The measurements were carried out using a Ti-Ir coated silicon cantilever with a spring constant of 2 N/m.

Figure 3.1(a) shows a 50 x 50 μm^2 non-contact topographic image of wings surface showing about 10-12μm long micro-structures distributed all over the surface in a semi-periodic manner. The long axes of all such islands in the scanned area are oriented in the same direction. The cantilever probes the same area twice by taking forward (trace) and reverse

(retrace) scans. Figure 3.1(a) and (b) show the trace and the retrace images respectively. It is clearly evident from these images that there is a loose structure at the bottom of the micro-structure which is being dragged along the tip during trace (Figure 3.1(a)) and is being swept back by the tip during retrace (Figure 3.1(b)).

Figure 3.1(c) shows a 2 x 2 μm^2 non-contact topographic image of a region as shown in Figure 3.1(a). Nanoscale bumps are distributed throughout the wing's surface in a non-periodic manner. These bumps are about 250 nm wide and 40-50 nm high. Figure 3.1(d) shows a 3-dimensional scan of the same region as in Figure 3.1(c).

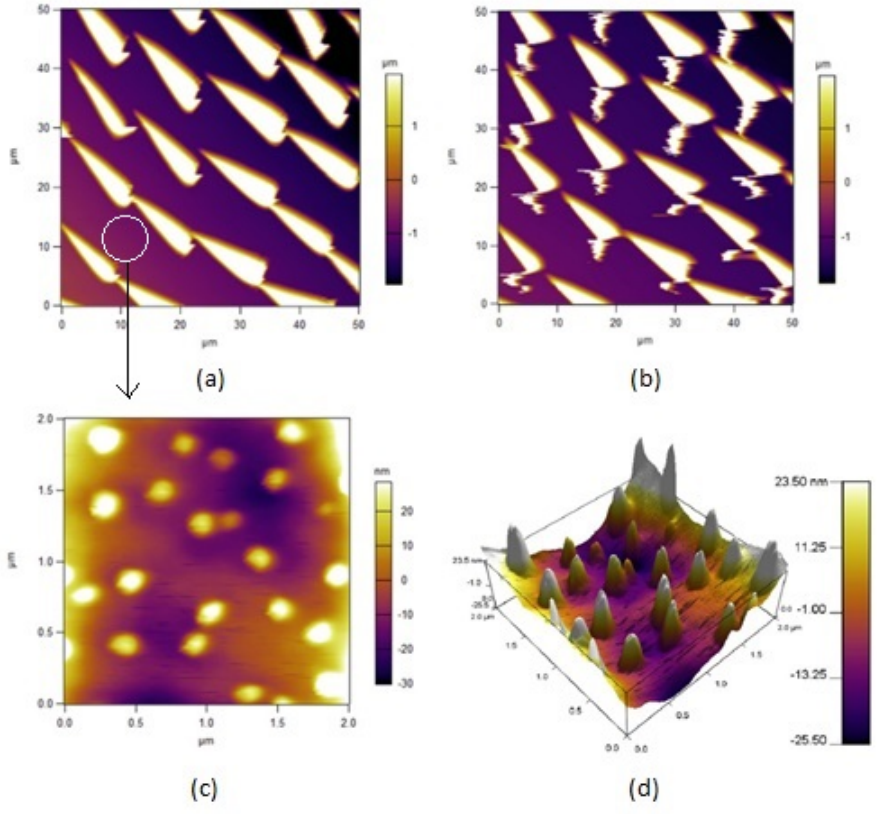

Figure 3.1: (a),(b) 50 x 50 μm^2 trace and retrace topographic image showing long micro-structures distributed in a semi-periodic manner respectively. (c)Non-contact topographic image of 2 x 2μm^2 area shown in (a) showing nano-scale bumps. (d)Three dimensional profile of the image in (c).

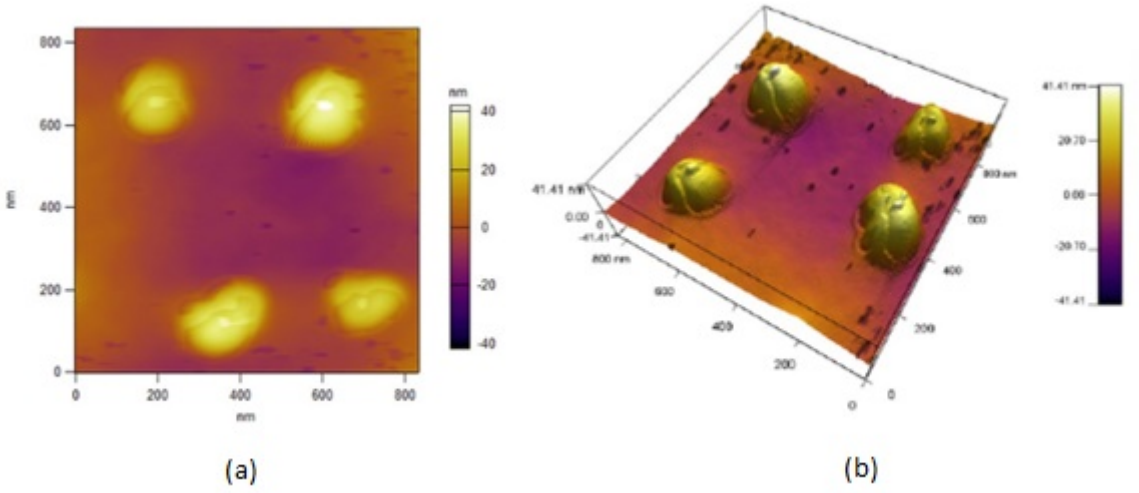

Figure 3.2: (a):Topographic image of randomly chosen four nano-bumps in a 800 x 800 nm^2 area. (b)Three dimensional profile of the image in (a)

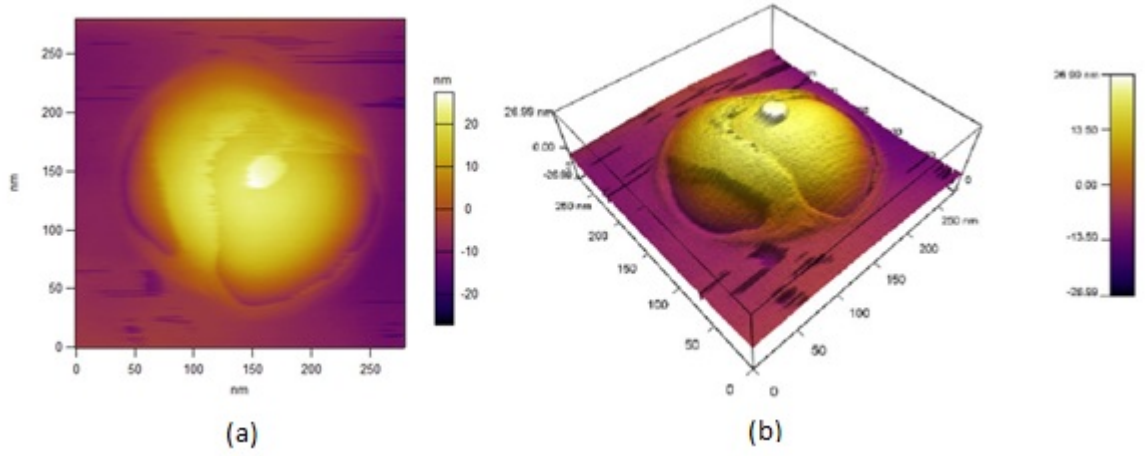

Figure 3.3: (a) Topographic image of a single bump in a 300 x 300 nm^2 area. (b)Three dimensional profile of the same image as in (a)

Figure 3.2(a) shows a 800 x 800 nm^2 non-contact topographic image randomly chosen four of the nanoscale bumps shown in Figure 3.1(c). Figure 3.3(a) and (b) shows a high resolution 2-D and 3-D topographic image of a single nano-bump respectively. It can be seen that all the nano-bumps have the same topography which comprises of a small protrusion in the middle, a layer on the bump with a cut on the left which is similar for all of the bumps.

The wings of Drosophila Melanogaster have micro-structures distributed on its surface in a semi-periodic manner which are 10-12 μm long and 5-6 μm high. The background matrix

is crowded with randomly distributed nano-bumps which are about 250 nm in width and 40-50 nm in height. Each one of these bumps has similar architecture in terms of a protrusion, a surrounding membrane with a cut which is in same direction for all of them. The origin and function of this specific architecture on the nano-scale bumps is a matter of curiosity. It would also be interesting to study at what stage of development this architecture begins to develop and if there is any structural correlation with its function.

Chapter 4

Microscopic modulation of mechanical properties of transparent insect's wings

We report on the measurement of local friction and adhesion of transparent insect wings using an atomic force microscope (AFM) cantilever down to nanometre length scales. We observe that the wing-surface is decorated with 10 μm long and 2 μm wide islands that have higher topographic height. The friction on the islands is two orders of magnitude higher than the back-ground while the adhesion on the islands is smaller. Furthermore, the high islands are decorated with ordered nano-wire-like structures while the background is full of randomly distributed granular nano-particles. Coherent optical diffraction through the wings produce a stable diffraction pattern revealing a quasi-periodic organization of the high islands over the entire wing. This suggests a long-range order in the modulation of friction and adhesion which is directly correlated with the topography. The measurements unravel superior functional design of complex wing surface and could find application in miniature biomimetic devices.

Insect wings are known to possess remarkable mechanical and optical properties. They are naturally engineered to be among the best materials with superior self-cleaning, anti-wetting, anti-bacterial properties and they exhibit bountiful varieties of exotic colour patterns [19, 20, 21, 22]. It is believed that naturally controlled nano-structuring of the wings' surface govern their remarkable properties [23, 24, 25]. In the past wide, various topographic micro-structures on diverse insect wings were probed, and their functionalities were investigated by employing a number of imaging and characterization techniques [19, 24, 25, 26]. With the development of high-resolution imaging capabilities, it has now

been possible to investigate the detailed structure of the wing-topography down to sub-micrometer length scales. Attempts have been made to mimic the naturally engineered structures in biological systems for enhancing the functionality of man-made devices and for synthesizing new materials [21, 28, 29, 30, 31, 32, 33]. However, owing to the diversity and complexity of the insect wings, a complete understanding of their sub-microscopic mechanical properties remained an unattained goal.

In the past, mechanical properties of certain insect wings have been measured by macroscopic measurement techniques, and the average friction and adhesion values on the wing surface were found to be low [20, 23, 34]. In this context, superior self-cleaning and anti-wetting properties of the insect wings were attributed to the measured low adhesion on the surface [20, 22, 23, 35]. However, the distribution of the mechanical properties down to nanometre length scales on transparent insect wings, an important information for understanding the rich functional properties and their structural origin, was not known. In this paper we report on the microscopic friction and adhesion properties of the transparent wings down to nanometre length scales using an atomic force microscope (AFM) cantilever. We show a strong spatial-modulation of frictional and adhesive properties on the wing which is directly correlated to its topographic modulation. We perform high resolution imaging of the high and low friction areas to understand the possible dependence of the mechanical properties on the distribution of surface roughness. From an analysis based on the model of Rumpf [36], we explain how the observed modulation of the mechanical properties might originate from the fine topographic structures [37]. Furthermore, by complementing these results with coherent optical diffraction experiments, we show that the microscopic modulation of friction and adhesion is distributed in a quasi-periodic fashion over the entire surface of the wing.

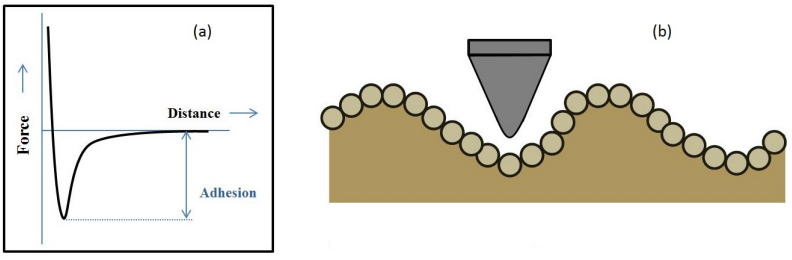

Figure 4.1: Schematic description of (a) a typical force curve obtained for adhesion force measurements using an AFM cantilever. (b) A surface with low local asperity and high hills and valleys. The AFM tip interacts differently to these during friction and adhesion measurements.

The wings have small ripples towards the edge that makes the surface near the edge lift out of plane. In order to make the wing sit flat on the surface we have pressed the wrinkled sides and rigidly fixed them on the slide with scotchtape. A section of around 3 mm x 3 mm flat region, anchored from all sides by tapes, was exposed where AFM measurements were performed.

Frictional forces were measured by bringing a Titanium-Iridium coated tip mounted at the end of a silicon cantilever in contact with the surface of a transparent wing of a rain-fly using Lateral Force Microscopy (as described in Section 2.1).In Figure 4.2(a) we demonstrate the frictional force distribution in an arbitrarily chosen area of 50x50 μm^2 on the surface of the wing. Remarkably, the tip encounters almost 70 times higer friction in the bright regions as compared to the dark regions. From the visual inspection it is clear that the relative friction is higher in some elongated islands of length 10 μm and width 2 μm. The separation between two nearest islands is 10 μm. About 10 such high-friction islands can be seen in Figure 4.2(a). The long axes of all such islands in the scanned area are oriented in the same direction.

In order to investigate the possible correlation of the modulation of friction with topographic modulation, we performed topographic imaging of the same area as shown in Figure 4.2(a). The topographic image is shown in Figure 4.2(b). By comparing the friction and the topographic maps, it becomes evident that the modulation in friction is correlated with the modulation in topography – Regions with higher topography offer higher friction to the tip.In order to investigate the correlation of the observed topographic modulation with other mechanical properties than friction, we measured distribution of the adhesive forces on the wing. For this measurement, the wing was loaded flat on a glass slide, and the measurement was carried out using a Ti-Ir coated silicon cantilever with a spring constant of 2N/m. First, the AFM tip was allowed to approach the surface with the feedback loop on. The approach stops as soon as the deflection of the cantilever reaches a pre-set value (the set point). From this point the tip is allowed to retract slowly, and the force required to pull the tip out of the attractive regime of the force curve is measured, and this is proportional to the adhesion force. This could be approximated to be equal to the depth of the attractive region of the force versus distance curve as shown in Figure 4.1(a). The force curve is recorded for a large number of points on the surface, and the adhesion force plotted as function of the position of the AFM tip gives the adhesion image. From the measurements carried out, it is observed that the adhesion force has a lower value on the high islands as compared to the background.

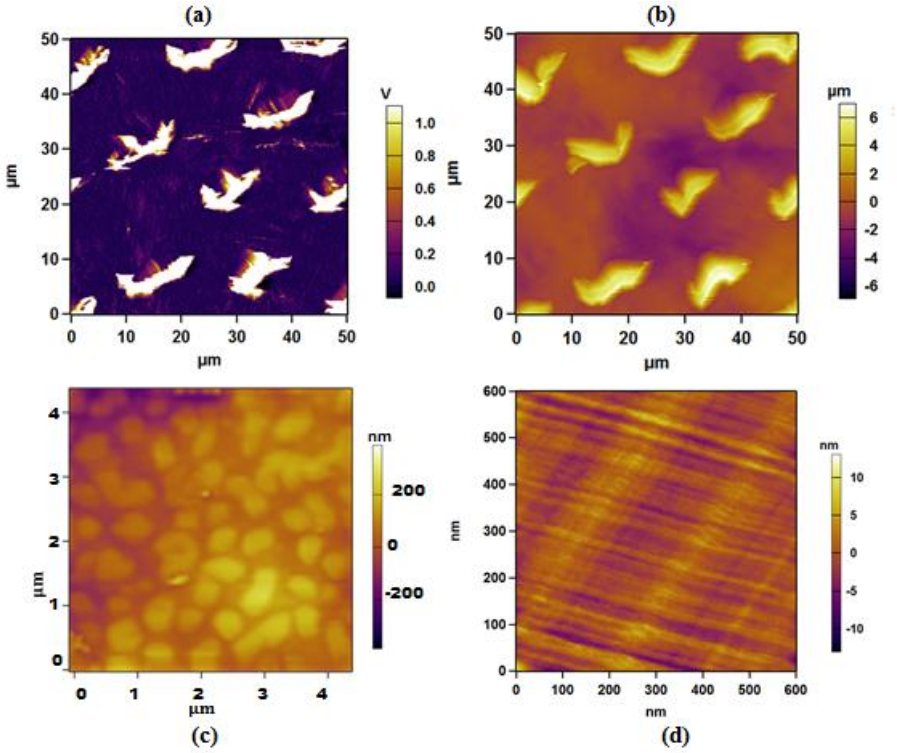

Figure 4.2: (a) Distribution of relative frictional forces on a 50 μm^2 area on the wing surface. (b) Topographic image of the same area as in (a) topographic height distribution. (c)Higher resolution topographic image of the back ground showing granular topography. (d) Nano-structures on top of one of the islands.

Figure 4.3(a) depicts the adhesion force map on a 16x8 μm^2 area that includes one island of higher friction. The force curve was recorded at 70x70 points on the given area for constructing this plot. Figure 4.3(b) shows the topographic image of the single island on which the measurement for Figure 4.3(a) was done. From a comparison between Figure 4.3(a) and Figure 4.3(b), it is evident that adhesive force experienced by the tip is significantly higher on the high island than on the background.

In Figure 4.2(a) we demonstrate the frictional force distribution in an arbitrarily chosen area of 50x50 μm^2 on the surface of the wing. Remarkably, the tip encounters almost 70 times higer friction in the bright regions as compared to the dark regions. From the visual inspection it is clear that the relative friction is higher in some elongated islands of length 10 μm and width 2 μm. The separation between two nearest islands is 10 μm. About 10 such high-friction islands can be seen in Figure 4.2(a). The long axes of all such islands in the scanned area are oriented in the same direction.

Since frictional and adhesion properties are believed to originate from sub-microscopic structural properties, we performed high resolution imaging on the wing surface down to nanometre length scales. The high friction and low adhesion islands show parallel nanowire-like structures of diameter 5 nm (Figure 4.2(d)). These wire-like structures are oriented perpendicular to the long axes of the islands. At certain locations thicker (diameter 10 nm) ridge-structures run perpendicular to the 5 nm diameter wires. One of the side-walls of each island is slanted and is decorated with the above-mentioned nano-wire-like structures. Such nano-structuring might or might not be present in the opposite wall– it is not clearly resolved due to the presence of a concave curvature in that wall and therefore the tip cannot probe the wall surface. In contrast, when we zoom into an area of 5x5 μm^2 in the background, we observe 300 nm 500 nm wide particles (Figure 4.2(c)). The high islands as well as the background was further imaged by a scanning electron microscope where the random distribution of the nano-particles in the background was also observed (Figure 4.4(c,d,e)).

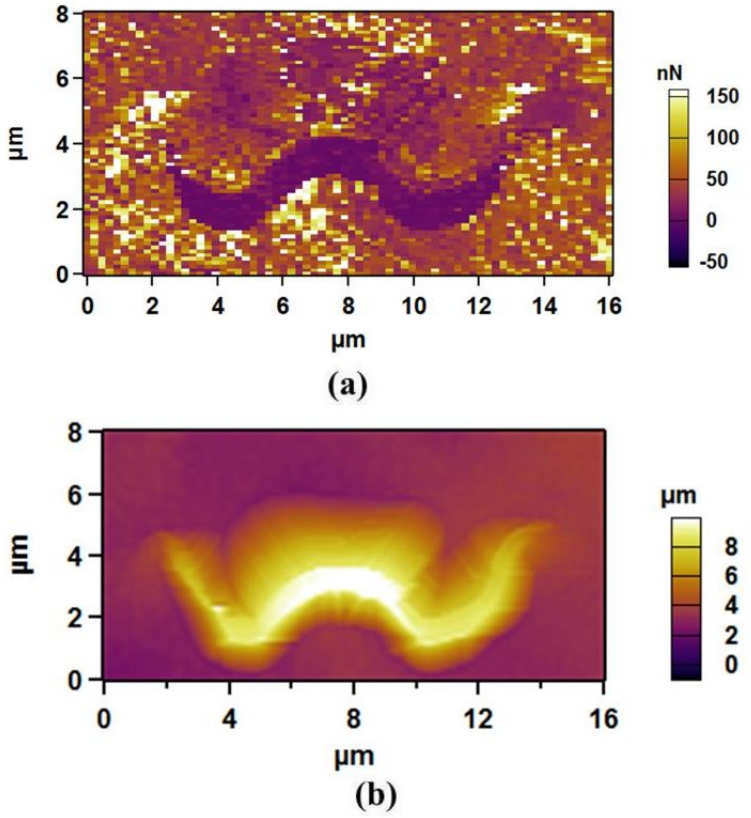

Figure 4.3: (a) Modulation of the adhesive forces in a 16 μm^2 area containing one high island. (b) Non-contact AFM topographic image of the single island as in (a).

It should be noted that in the past adhesion force mapping was carried out on the wings of Drosophila Melanogaster and it was found that the wings had nano-scale bumps on which the adhesion was not significantly different from the surrounding membrane [38]. From our measurements it is clear that the friction is higher but adhesion is lower on the islands compared to the background. It is common wisdom that friction is related to the roughness of the surface. From past theoretical studies it is also known that surface roughness may also influence adhesion properties. Within the theoretical model developed by Rumpf [36], the adhesion force between a particle and a surface is given by

$$F_{adh} = \frac{A_H R}{6D_o}\left[\frac{r}{r+R} + \frac{1}{(1+\frac{r}{D_o})^2}\right] \tag{4.1}$$

where R refers to the particle radius, r is the asperity radius on the surface, A_H is Hamekar constant and D_o is the minimum distance between sphere and asperity (inter-atomic spacing). If the asperity radius on the surface is small, the AFM tip, whose apex may be approximated to be a particle, will experience a lower adhesion. Comparing the structural details of Figure 4.2(c) and Figure 4.2(d) it is clear that the effective value of r is higher on the background than on the high islands: The mean asperity radius on the islands is around 5 nm while the bigger granular structures in the background may lead to a higher value of r. This explains the lower adhesion on the high islands as compared to the background. However, friction between the AFM tip and the surface is also affected by the larger hills and valleys existing on a surface. As shown in Figure 4.1(b), the small circular structures on the sample around the tip will contribute to adhesion but the larger hill-like structures will not contribute for a given point on the surface where the adhesion is measured. However, the larger hill-like structures should contribute strongly to friction, since friction measurements involve dragging the tip laterally along the surface. The topography on the islands has several hills and valleys as seen in the image of a single island in Figure 4.3(b) leading to a higher friction on the valleys. Such modulation of topography does not exist in the background.

From the above measurements it is clear that the surface of the wings has well defined islands that have greater height than the background, and have higher friction and lower adhesion than the background. It is known that lower adhesion of the wings give rise to their self-cleaning properties like in lotus leaves [19, 20, 21, 39, 40, 41, 42, 43]. The specific architecture and enhanced friction might grant the insects an aerodynamic advantage during strong winds [44]. However, it is remarkable that such properties are localized at certain

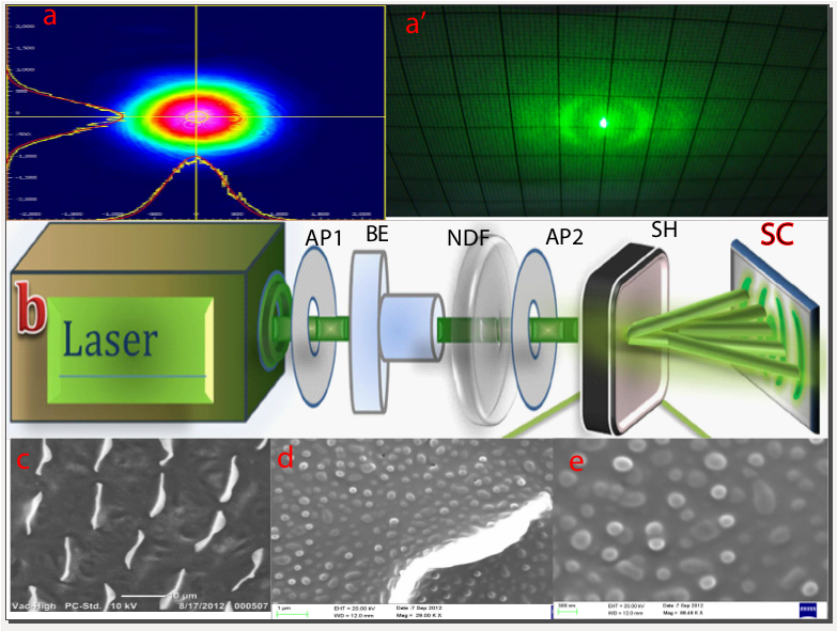

Figure 4.4: (a) Incident beam profiles for a green solid-state laser($\lambda = 523nm$). (a′) digital photograph of the diffraction pattern on the screen (b) schematic of the set-up with various components SH:wing sample hold ; AP1,AP2: iris; C: beam expander; SC: screen and NDF: ND filter wheel. (c)Micro-structures with 10 micrometer scale bar (d) Single structure with nano-structure patterning (e) nano-structure arrangement with 300 nm scale bar.

specific points. It appears that additional volume is needed for required nano-structuring that facilitates the desired mechanical properties. However, larger volumes lead to increase in the total mass of the wing which is disadvantageous for flight. Hence, we may surmise that the advantageous mechanical properties have been distributed over the wing such that the total mass is minimized without compromising on the advantages.

In order to probe the distribution of the islands over a large area up to millimetre length scales on the wing, we have performed optical diffraction imaging of a pristine wing sample [45]. Due to optical transparency, these wings exhibit a stable diffraction pattern with coherent laser beams of different types. The experimental set up is shown in Figure 4.4. A green laser (spot size = 2 mm) was irradiated on the wing mounted on the path of the laser, and the diffraction pattern was captured on a screen that was mounted 20.5 cm away from the wing. This produced a characteristic pattern with a central bright spot and two higher order maxima as shown in Figure 4.4(a). From the average distance between these maxima we estimated an existence of quasi-periodicity of the micro-structures with an average spatial period of 10 μm over mm length scale. This suggests the existence of a quasi periodic distribution of thicker islands, and consequently, a long-range quasi periodic modulation of

friction and adhesion on the wing surface is also established.

To conclude, we have observed strong spatial modulation of nano-scale friction and adhesion on the transparent insect wings. There are microscopic islands composed of nanowire-like structures on which the AFM tip experiences higher friction and lower adhesion as compared to the background which is decorated with granular nano-particles. The nano-scale mechanical properties of the wings are correlated with the topographic features over the entire wing. Optical diffraction experiments demonstrate that the islands responsible for modulation of friction and adhesion exhibit long range spatial order. In addition to the outstanding aerodynamic, self-cleaning, and anti-wetting properties, the observed unique nano-scale mechanical properties might provide new design ideas for biomimetic miniature devices with enhanced functionalities.

Chapter 5

High Temperature Ferroelectricity in $SrTiO_3$ crystals

$SrTiO_3$ is known to be an incipient ferroelectric. It is thought that ferroelectric stability in $SrTiO_3$ is suppressed by a delicate competition with quantum fluctuation and antiferrodistortion. The ferroelectric phase can, however, be stabilized by doping, isotope manipulation and strain engineering etc. Till date ferroelectricity in $SrTiO_3$ thin films was observed to exist up to room temperature – that was when the films were grown on specially engineered substrates using complex growth techniques. It was possible to write and erase ferroelectric domains on the specially engineered films at room temperature. Here, we show remarkably similar ferroelectric behavior in bulk (110) single crystals of $SrTiO_3$ with no special engineering well above room temperature using piezoresponse force microscopy. Hysteretic switching of local electric polarization was observed and electrically active domains could be written and erased using lithographic techniques at remarkably high temperatures up to $420K$.

Strontium titanate ($SrTiO_3$) has found wide range of application as a substrate for the epitaxial growth of functional oxide thin films because of its high dielectric constant.[46] The list of oxides that have been successfully grown on $SrTiO_3$ with high degree of epitaxy includes high temperature ceramic superconductors, colossal magnetoresitive manganites, itinerant ferromagnets etc.[47, 48, 49] More recently, it has been shown that a two-dimensional electron gas is formed under certain conditions at the interface of insulating $SrTiO_3$ and insulating $LaAlO_3$ (LAO) where novel interplay between superconductivity and magnetism has been reported.[47, 50] Therefore, the bulk and surface properties of $SrTiO_3$ have attracted considerable attention in contemporary condensed matter physics.

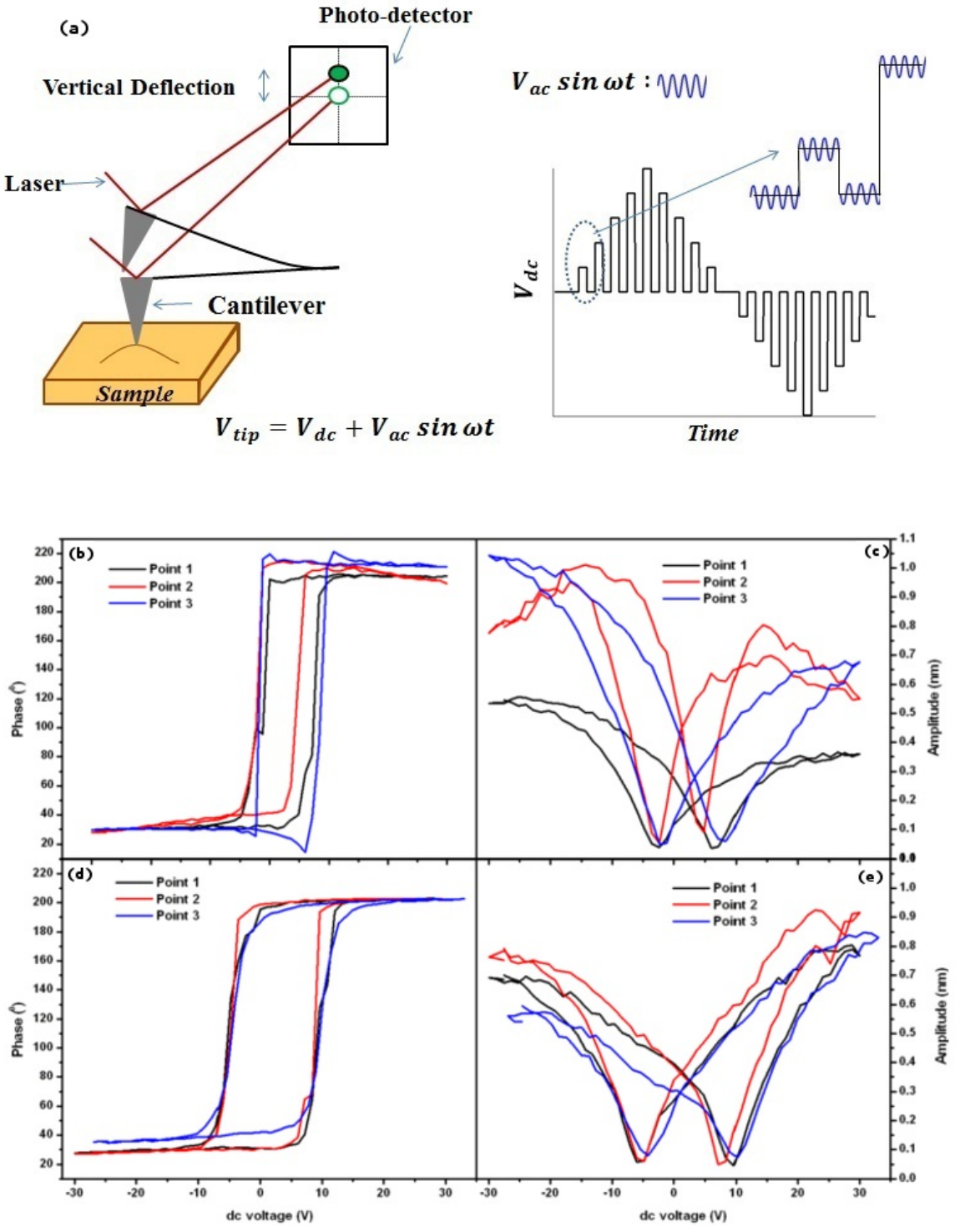

Figure 5.1: (a) Schematic description of the PFM technique. The switching waveform in the DART-PFM switching spectroscopic mode is also shown.(b) PFM phase hysteresis and (c) butterfly loops at $300K$ at three different points in the "off" state. (d) PFM phase hysteresis and (e) butterfly loops at $420K$ at three different points in the "off" state as in (d).

$SrTiO_3$ crystallizes in the cubic perovskite structure in its paraelectric phase and is known to lead to a cubic to antiferrodistortive phase transition at $105K$.[51, 52, 53] From first principle calculations, it was inferred that $SrTiO_3$ might possibly have a low temperature $(40K)$ ferroelectric phase under hydrostatic pressure or strain.[54] As the ferroelectric phase was not experimentally detected it was believed that quantum fluctuations forbade a stable ferroelectric phase at low temperatures.[53, 55] The idea of quantum fluctuations was further supported by the observation of a ferroelectric phase when the oxygen of $SrTiO_3$ was replaced with the ^{18}O isotope.[56] However, more recently, it has been shown that ferroelectricity in epitaxial thin films of $SrTiO_3$ could be induced by strain engineering.[57, 58, 59, 60] Nevertheless, the consensus has been that the ferroelectric transition cannot be observed in pure bulk crystals of $SrTiO_3$. However, more recently, by superior thin film deposition methods a room temperature ferroelectric phase of strain-free $SrTiO_3$ film could be achieved.[109] The observation of ferroelectricity in strain free $SrTiO_3$ naturally leads to the idea that room temperature ferroelectricity might, in principle, be possible in bulk single crystal of $SrTiO_3$ as well. In fact, from computer simulation [62], low-energy electron diffraction[63] and surface x-ray diffraction[64] it was argued that surface ferroelectricity in a few monolayers of bulk $SrTiO_3$ should be possible. In this Letter,we show that the surface of $SrTiO_3$ shows hysteretic switching of polarization with DC bias. It is also possible to write and erase ferroelectric domains on single crystals of $SrTiO_3$ at remarkably high temperatures up to $420K$ indicating the existence of ferroelectricity in bulk $SrTiO_3$ at such high temperatures.

In order to probe ferroelectricity in bulk single crystals of $SrTiO_3$, we employed piezoresponse force microscopy (PFM) and switching spectroscopy. In this measurement a cantilever with a conducting tip is mounted in an atomic force microscope (AFM) and is electrically connected to a DC high-voltage (up to $220V$) amplifier and a lock-in amplifier. The lock-in amplifier sends a sinusoidal voltage $(V_{ac}sinwt)$ to the cantilever, which is brought in contact with the sample during PFM measurements. The amplitude response from the cantilever in the contact mode is probed as function of w in order to find the in-contact resonance frequency (w_r) of the cantilever. The measurements are performed at w_r in order to obtain maximum sensitivity. It is believed that a 180^0 switching of the phase of the response signal from the cantilever is a signature of ferroelectricity. The switching behaviour should also be hysteretic when a DC voltage (V_{dc}) is swept on the cantilever. This is attributed to the switching of the ferroelectric domains in the ferroelectrics. On the other hand, hysteretic amplitude vs. voltage curve, also known as a "butterfly loop", is the hallmark of piezoelectricity.

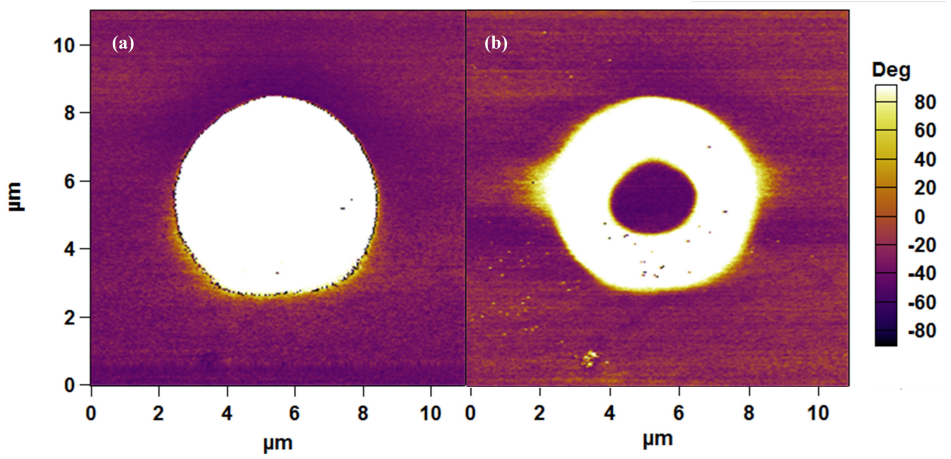

Figure 5.2: (a) Phase image of a circular domain written at room temperature by applying $+30V$ and (b) phase image of the domain after applying $-30V$ at the center of the domain written in (a).

A (110) single crystal of $SrTiO_3$ (from MTI Corporation) was cut into a $3mm \times 3mm$ piece and was loaded on a metallic sample holder. The sample holder was mounted on the sample stage of an AFM where the metallic sample holder was internally connected to the ground of the high voltage amplifier. In order to measure temperature dependence of the data, we had mounted a heating kit in the AFM. The sample was in direct thermal connection with the hot surface of the heating kit. The heating kit was capable of raising the sample temperature up to $570K$. The cantilevers that were used for these measurements were made of silicon and coated with $5nm$ of titanium and $20nm$ of iridium. The spring constant of the cantilever was $2N/m$ with its natural resonance frequency in air around $70kHz$. The in-contact resonance frequency of the cantilever on $SrTiO_3$ was found to be in the range of $290 - 310kHz$.

It should be noted that hysteretic phase switching and butterfly loops may also originate from reasons other than ferroelectricity and piezoelectricity in PFM.[65, 66] One of the possible reasons could be the local electrostatic effects. In order to mitigate this effect, all the spectroscopic data reported here were measured by employing a switching spectroscopy PFM (SSPFM) protocol pioneered by Jesse *et.al.*, where a sequence of DC voltages in triangular saw tooth form was applied between the conducting cantilever and the $SrTiO_3$ as shown in Figure 5.1(a).[67, 68] The measurement was carried out in the "off" state of the pulses. As shown in Appendix A, there is a significant difference between the "on" state and the "off" state data. This suggests that the local electrostatic effects have been minimised

during the spectroscopic measurements. The electro-chemical response in the presence of a high DC bias may also mimic the ferroelectric like hysteresis effects. Usually one clear signature of an electrochemical reaction is the formation of topographic structures on the surface.[65, 66] However, in the present case, no topographic structure growth was noticed (see Appendix A).

In Figure 5.1 (b) and Figure 5.1 (d), we show the phase voltage hysteresis obtained at $300K$ and $420K$ respectively at three different points. From a visual inspection of the data, it is clear that the phase switches by 180^o with a coercive voltage of approximately $10V$. The switching is sharp at $10V$ beyond which the hysteresis curve saturates. As shown in Figure 5.1(c) and Figure 5.1(e), the amplitude vs. V_{dc} curves also show hysteresis and form "butterfly loop" at $300K$ and $420K$ respectively at three different points. This is believed to be the signature of piezoelectricity. By analysing the data, we have extracted the value of the piezoelectric coefficient which is $0.422nm/V$ at $300K$. For temperatures above $420K$, no piezoelectric or ferroelectric like response was observed on $SrTiO_3$.

As it has been discussed before, based on the observation of hysteresis curves alone the ferroelectric phase of $SrTiO_3$ cannot be confirmed. Therefore we have attempted to write ferroelectric domains on $SrTiO_3$ using a conducting cantilever. A tip made of Silicon coated with $5nm$ of titanium and $20nm$ of iridium and spring constant $2N/m$ was used to write a circular domain using lithography. A circular domain was written by applying $+30V$ on $11\mu m \times 11\mu m$ area on the surface of bulk $SrTiO_3$ crystal. After writing the domain the area was scanned in regular PFM imaging mode. The height image did not show any modification while a bright circular domain was clearly visible in the phase image (Figure 5.2(a)). After that we applied a negative voltage ($-30V$) on a smaller concentric circular area inside the bright domain. When we imaged the domain again after the second writing, we observed a dark spot at the center of the bright domain. The phase difference between the bright region and the dark region was 180^o indicating that the polarization at the central dark region was reversed due to the application of a negative voltage. Therefore, we have successfully written and erased a ferroelectric domain on the surface of bulk $SrTiO_3$ crystal.

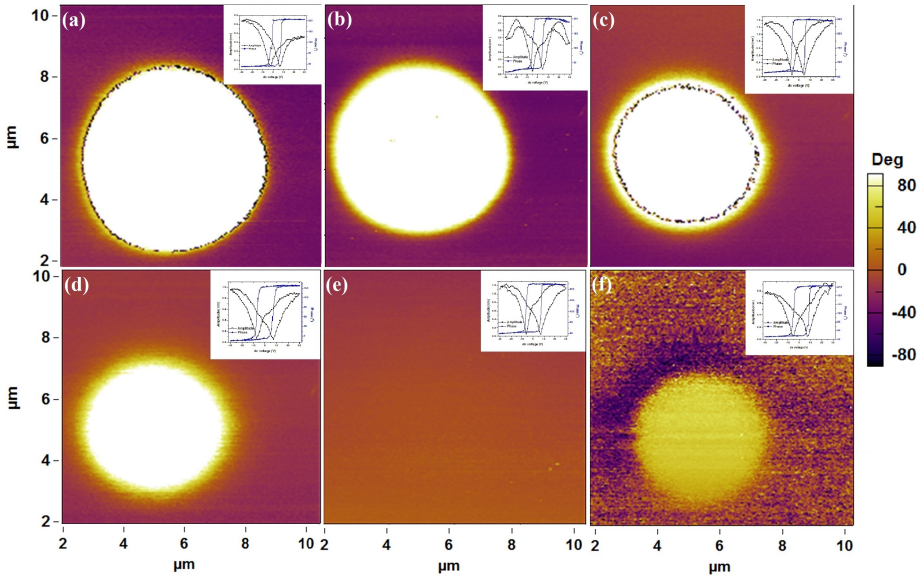

Figure 5.3: (a) A circular domain written on bulk $SrTiO_3$ with $+30V$ on a $8\mu m \times 8\mu m$ area at $300K$. The PFM Phase images of the domain at different temperatures: (b) $330K$ (c) $360K$ (d) $390K$ (e) $420K$; (f) Phase image (at $300K$ of the domain written with $+30V$ at $440K$ and then immediately cooling the sample down to $300K$.

We also attempted to image the natural ferroelectric domains by regular and vector PFM. However, distinct domain structures were not observed. It is possible that the natural domains do exist but we cannot image them by PFM due to large tip size ($\sim$ 25nm) that limits the lateral resolution of the images.

In order to estimate the Curie temperature of the ferroelectric phase, temperature dependence of an artificially written circular domain was studied. We first wrote the circular domain of diameter 6 μm by PFM lithography with an applied voltage of $+30V$ on $SrTiO_3$ at $300K$. The domain was then imaged using DART PFM at different temperatures as shown in Figure 5.3: $300K$ (Figure 5.3(a)), $330K$ (Figure 5.3(b)), $360K$ (Figure 5.3(c)), $390K$ (Figure 5.3(d)) and $420K$ (Figure 5.3(e)). From visual inspection alone it is clear that with increase in temperature the domain structure written at $300K$ starts disappearing, the diameter shrinks, and it disappears completely at $420K$ (also see Appendix A). After imaging the domain at every temperature we have also performed spectroscopic measurements in order to investigate the evolution of the relevant parameters like the coercive field and the piezoelectric constant. The spectroscopic data are presented as insets in Figure 5.3. Surprisingly, no systematic temperature dependence of the ferroelectric/piezoelectric

parameters was noticed. However, no spectroscopic piezo and ferroelectric response on temperature above $440K$ could be found.

In order to investigate the time dynamics of the domains we have also measured the relaxation time (the time over which the domain completely disappears) of the domains. The domain survives for 12-14 hours at room temperature (see appendeix 1). As the temperature was increased from $300K$ up to $420K$, the relaxation time significantly decreases from 12-14 hours to 2-3 minutes. It was possible to write a domain even at $440K$ but due to very short lifetime of the domain at this temperature the domain relaxed before it could be imaged. However, when we wrote the domain at $440K$ and immediately cooled the sample down, the domain did not fully relax and it was possible to image the domain at room temperature (Figure 5.3(f)).

From the data presented above it is clear that the surface of $SrTiO_3$ is electrically active and the electrical response is hysteretic. In this context it should be noted that in the past the controlled bilayers of $SrTiO_3$ and $LaAlO_3$ were also shown to be electrically active where the hysteresis effects were observed and electric domains were written.[69, 70, 71] Such behaviour was attributed to the existence of an exotic interface in the $SrTiO_3$/$LaAlO_3$ bilayers. Since we observe similar effects on the surface of bulk $SrTiO_3$ alone, the origin of such effects in the $SrTiO_3$/$LaAlO_3$ bilayers should be revisited.

The surprising observation of very high temperature ferroelectricity in pure crystals of $SrTiO_3$ is not understood at present and further theoretical investigation is required. Qualitatively, the observation may be attributed to a voltage induced strain[72] on the surface developed during the spectroscopic measurement and domain writing. When a DC voltage is applied on the surface through the conductive tip, the effective electric field is very large. At such high electric fields the lattice may distort in the direction of the applied field due to electrostriction. This distortion results in a change in the Ti-O bond length. This change breaks the inherent centrosymmetric nature of the cubic crystal structure of $SrTiO_3$ and induces electric polarization. It is not surprising that the lifetime of the induced strain is temperature dependent as at higher temperature the field-induced distortion should relax faster. The important thing to note, however, here is that the induced polarization has a rather long lifetime at room temperature. The microscopic mechanism leading to such long relaxation time should be investigated.

In conclusion, we have performed piezoresponse force microscopy on (110) single crystals

of $SrTiO_3$ and found the evidence of a ferroelectric phase up to $440K$. It was possible to write and erase electric domains using conducting cantilevers on the surface of the crystals. From the temperature dependence of the hysteresis effects and the electric domains we conclude that the ferroelectric Curie temperature is more than $440K$. Based on the results presented here the origin of the exotic electric behaviour of the $SrTiO_3/LaAlO_3$ interfaces should be revisited.

Chapter 6

Evidence of strong ferroelectricity in a thermoelectric semiconductor

Owing to their potential to efficiently convert waste heat into electricity, nanostructured thermoelectrics have been enjoying a renaissance period in recent times. Instead of second phase nanostructuring if naturally occurring electrically active nano-domains could facilitate the control of the interdependent thermoelectric parameters, that would not only open up new directions for achieving higher thermoelectric performance through domain engineering but also give the flexibility of tuning the thermoelectric properties by electric field. In order to accomplish this, it is most important to first identify the existing high performance thermoelectric materials containing such electrically active nano-domains and study the role of the domains in generating superior thermoelectricity. Herein, through the direct measurement of local polarization switching, for the first time, we show that the thermoelectric semiconductor $AgSbSe_2$ has local ferroelectric ordering . Using piezo-response force microscopy, we demonstrate the existence of nanometer scale ferroelectric domains that can be switched by external electric field.

Thermoelectric materials enable direct and reversible conversion of untapped heat into electrical energy and will play a significant role in the future energy management. The effectiveness of thermoelectric materials is evaluated by a dimensionless figure of merit, $zT = \sigma S^2 T/(k_{el} + k_{lat})$, where σ, S, T, k_{el} and k_{lat} are electric conductivity, Seebeck coefficient, temperature, electronic thermal conductivity and lattice thermal conductivity respectively [73, 74, 75, 76, 77, 78]. Recently, the field of thermoelectricity witnessed a revolution with the emergence of wide variety of novel materials with increasingly high zT[79, 80, 81, 82, 83, 84]. For increased zT, the materials need to have either high power

factor (σS^2) or low thermal conductivity (k) or both at the same time. In the past, the increase in zT was mainly accomplished by either lowering the dimensionality of the systems or by the introduction of second phase nanostructures in the matrix of existing thermoelectrics[79, 82, 83]. Infact, remarkable decrease in k_{lat} has been achieved via enhanced phonon scattering by solid solution point defects, second phase nanoprecipitates and meso-scale grain boundaries[85]. However, complex technical issues involved with the synthesis of efficient materials with tailored nanostructures and low dimensional nanomaterials; and their thermal instability have limited their application. Therefore, improvement of thermoelectric performance through novel technological innovation has remained to be an outstanding issue.

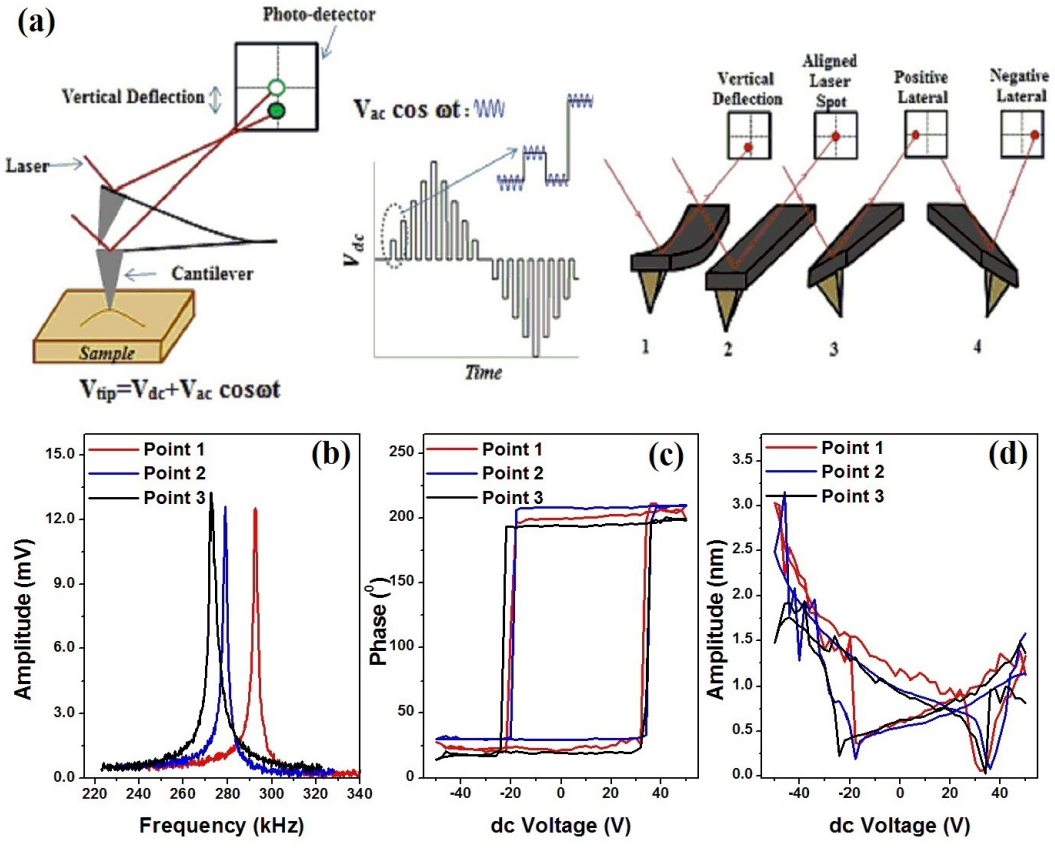

Figure 6.1: Direct evidence of the ferroelectric and piezoelectric response of $AgSbSe_2$ using a conductive Pt/Ir coated tip studied by Piezoresponce force microscopy (PFM). (a) Schematic of the PFM technique presenting the switching waveform in the DART PFM spectroscopic mode and the tip movement in Vector PFM mode. (b) Tuning of the conducting AFM cantilever in DART PFM mode prior to spectroscopic measurements. (c) PFM phase hysteresis loop and (d) butterfly loop measured at three different points in the "off"-state.

Investigation of the thermoelectric property of ferroelectric materials was considered in several contexts in the past. For example, ferroelectric Aurivillius phase, $Bi_4Ti_3O_{12}$, exhibited low thermal conductivity.[86] Single crystal of the relaxor ferroelectric oxide, $Sr_{1-x}Ba_xNb_2O_6$, showed low thermal conductivity and high power factor[87]. In relaxor ferroelectrics, nanopolar regions associated with intrinsic localized phonon modes provide glass-like phonon characteristics due to extensive phonon scattering[87]. In the lead chalcogenides, which are known to be high performance thermoelectric materials, local ferroelectric distortion has been observed by pair distribution function analysis of temperature dependent neutron diffraction data[88]. Using combination of inelastic neutron scattering and first principle calculations, strong anharmonic coupling between ferroelectric transverse optic mode and longitudinal acoustic modes have been evidenced in $PbTe$, which has been shown to be important for low thermal conductivity[89]. In certain systems, it was found that the itinerant electrons responsible for electrical conductivity were strongly coupled with the ferroelectric polarization [87, 90]. Therefore, in principle, by tuning ferroelectric properties it should also be possible to tune electrical properties, hence thermoelectric properties, in those systems[91]. Consequently, the ferroelectric materials with high electrical conductivity could be potential superior thermoelectric materials. In such systems, the nano-meter scale ferroelectric domain boundaries could act as potential scatterers of the mid/long mean free path phonons thereby limiting the thermal conductivity and enhancing zT. However, complete understanding of the correlation between ferroelectric and thermoelectric properties, so far, has remained elusive. This understanding is extremely important in order to be able to design novel materials with superior thermoelectric properties by hitherto unexplored techniques like engineering of ferroelectricity in semiconductors. Investigating the possibility of the existence of ferroelectric ordering in novel thermoelectric materials is, therefore, a major step forward to this direction.

Here, we present the existence of ferroelectricity in a new thermoelectric semiconductor $AgSbSe_2$, which crystallizes in cubic rock salt structure (space group, $Fm-3m$) with disorderd Ag and Sb positions. $AgSbSe_2$ is a p-type semiconductor that shows high zT of $\sim$ 1.2 when properly doped[92, 93]. The high zT was attributed to enhance electrical conductivity and low lattice thermal conductivity. The low lattice thermal conductivity arises due to the presence of high degree of anharmonicity in the $Sb-Se$ bond[94, 95]. Our observation of the existence of strong local ferroelectricity in $AgSbSe_2$ indicates that enhanced phonon scattering might also emerge from the nano-meter sized ferroelectric domain walls. The contribution of phonon scattering originating from different processes is expected to add up linearly and give rise to a net effective thermal conductivity. Within

the scope of the thermal conductivity measurement technique employed by Guin $et.al.$[94], selective measurement of different types of scattering could not be performed.

In order to investigate ferroelectric properties of $AgSbSe_2$, we employed piezo-response force microscopy (PFM). A schematic diagram describing the experimental details has been provided in Figure 6.1(a). We engaged a conductive tip mounted on a conductive cantilever on the surface of a rectangular piece of $AgSbSe_2$. For probing the piezoresponse of the microscopic region underneath the tip, an ac voltage V_{ac} was applied between the tip and the sample mounted on a metal piece which was directly connected to the ground of the voltage source. The frequency of V_{ac} was swept and the amplitude response of the cantilever in the contact mode was recorded in order to identify the contact resonance frequency of the cantilever on the sample. All the measurements presented in this paper were performed at the contact resonance frequency in order to achieve highest sensitivity. As shown in Figure 6.1(b), the contact resonance frequency varied between 270 kHz to 300 kHz during our measurements.

For PFM spectroscopy, the ac voltage $V = V_{ac}cos\omega t$ is mixed with a dc voltage (V_{dc}) and the sum $V_{tip} = V_{dc} + V_{ac}cos\omega t$ is applied between the tip and the sample. If the sample is piezoelectric, the area underneath the tip will be deformed due to the application of the electric field. Since the applied field has a periodic component, the amplitude of deformation can be written as $A = A_0 + A_\omega cos(\omega t + \phi)$, where ϕ is the phase difference between the applied field and the amplitude response. ϕ gives information about the electric polarization direction below the tip. Depending on the direction of the applied V_{dc}, the polarization underneath the tip switches direction. This is expected to give rise to a 180^0 shift in ϕ vs V_{dc} curve as passes through $V_{dc} = 0$. In general, for ferroelectric switching, the phase ϕ switches hysteretically and shows a finite coercive voltage. In Figure 6.1(c) we show the hysteresis loops obtained at three different points on $AgSbSe_2$. The hysteretic 180^0 phase switching is clearly visible. For piezoelectric samples, when amplitude A_ω is plotted against the sweeping V_{dc}, the curve is expected to be hysteretic resembling a butterfly. This is called a "butterfly loop" which is traditionally considered to be a hallmark of piezoelectricity. The representative butterfly loops measured at three different points on $AgSbSe_2$ are shown in Figure 6.1(d)

Observation of hysteretic phase switching and "butterfly loops" indicate that $AgSbSe_2$ has ferroelectric and piezoelectric properties. However, it should also be noted that such hysteresis in phase and amplitude may also arise from electrostatic and electrochemical

effects[96]. In order to minimize the role of the electrostatic effects, all the measurements were performed following SS-PFM (switching spectroscopy piezoresponse force microscopy) pioneered by Jesse $et.al.$[97, 98]. In this method, instead of sweeping V_{dc} continuously, it is applied in sequence of pulses and the phase and amplitude measurements are done in the "off"-states of the pulses. The difference between the "on"-state and the "off"-state measurement results is significant indicating that the electrostatic effects have been minimized in the "off"-state measurements. The possibility of electrochemical reactions under the tip is ruled out by topographic imaging after the spectroscopic measurements, where we do not observe any topographic modification that is usually expected to result from tip-induced electrochemical processes[96]. However, ruling out the above-mentioned possibilities with absolute certainty may not be possible by spectroscopic measurements alone. In addition to the hysteretic switching effects, the observation of domains on the sample surface would be unambiguous proof of ferroelectricity. We present the observation of ferroelectric domains by PFM imaging in the following section.

PFM imaging was done by bringing the tip in contact with the sample, applying the voltage V_{ac} on the tip and scanning the tip on the sample while keeping the deflection of the cantilever constant. If the electric polarization is opposite in two different domains, the measured value of ϕ varies by 180^0 between the two domains. By plotting the magnitude of ϕ as a function of the position of the tip, a PFM image exhibiting the distribution of ferroelectric domains on the sample surface is constructed. During PFM imaging the resonance frequency might shift as the cantilever rubs against the surface and interacts differently with the sample at different points. In order to track the contact-resonance in real time the measurements were done in so-called DART (dual ac resonance tracking) mode[100]. In Figure 6.2(a) we show the topographic image of a $2\mu m$ x $2\mu m$ area. In Figure 6.2(b) we show the phase image corresponding to the same area. The phase image shows regions with high (bright) and low (dark) values of ϕ. From the bright to the dark region the phase ϕ shifts by 180^o indicating that the bright and dark regions are respectively 'up' polarized and 'down' polarized ferroelectric domains.

In the imaging method described above only the vertical amplitude and phase response on the photodiode are recorded. The image thus obtained gives information about the components of electric polarization along the directions parallel and antiparallel to the axis of the tip. By probing the lateral deflection of the cantilever it is also possible to image the domains where the polarization axis remains on the plane of the sample surface. The images

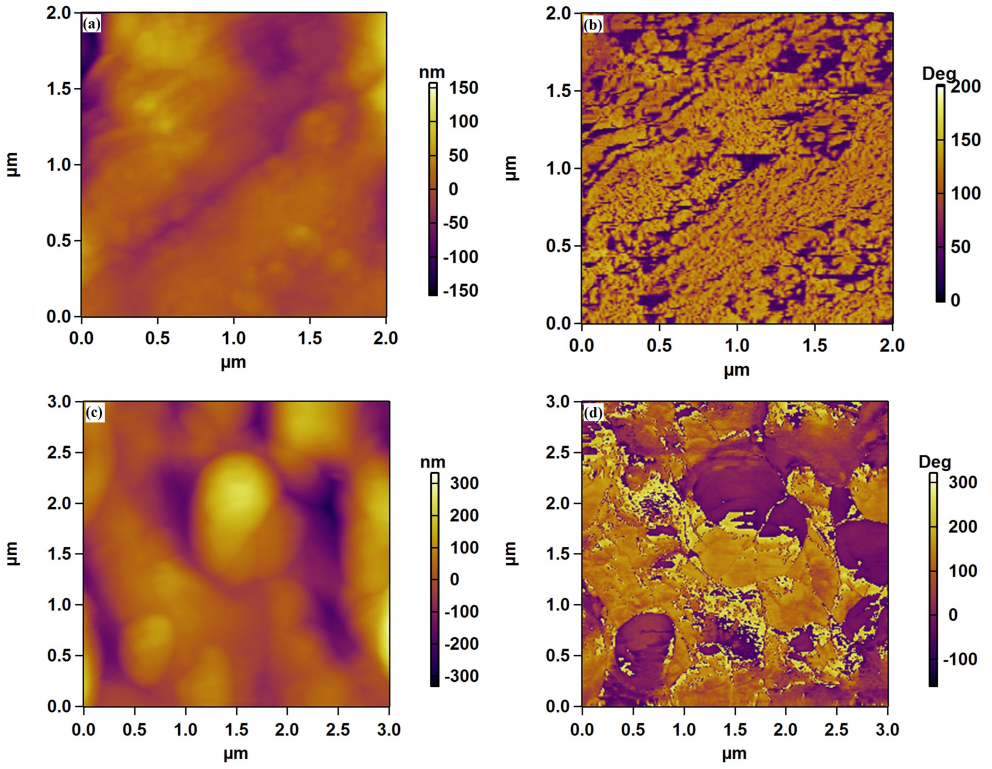

Figure 6.2: (a) Topography of a $2\mu m \times 2\mu m$ area on the sample. (b) PFM phase image showing nanometer scale domains in the same area as in (a). (c) Topography of a $3\mu m \times 3\mu m$ area on the sample. (d) Lateral PFM phase image showing nanometer scale domains in the same area as in (c).

of the lateral domains of a $3\mu m$ x $3\mu m$ area (topography shown in Figure 6.2(c)) is presented in Figure 6.2(d). Bright and dark regions comprising of domains of different electric polarization are clearly visible in the image. There is absolutely no correlation between the topographic and the phase image confirming that the phase image is not affected by the topography.

From the above results it can be inferred that $AgSbSe_2$ has local ferroelectric properties. Since $AgSbSe_2$ crystallizes in the centro-symmetric structure, the observation of ferroelectricity is surprising. It is therefore necessary to understand the origin of ferroelectricity in $AgSbSe_2$.

$AgSbSe_2$ is a member of cubic $I-V-VI_2$, where I = Cu, Ag, Au or alkali metal; V = As, Sb, Bi; and VI = Se, Te. In $AgSbSe_2$, the valence electronic configuration of Sb is $5s^2 5p^3$, where only $5p^3$ electrons take part in the formation of bonds with the Se valence electrons,

while the beguiling $5s^2$ electrons of Sb form lone pairs. Such ns^2 lone pairs electrons are often found to effective to distort the local structure, resulting in local dipole in the global centro-symmetric structure[88, 101, 102, 103, 104]. Thus, lone pair induced local distortion in the structure may gives rise to ferroelectric properties in $AgSbSe_2$.

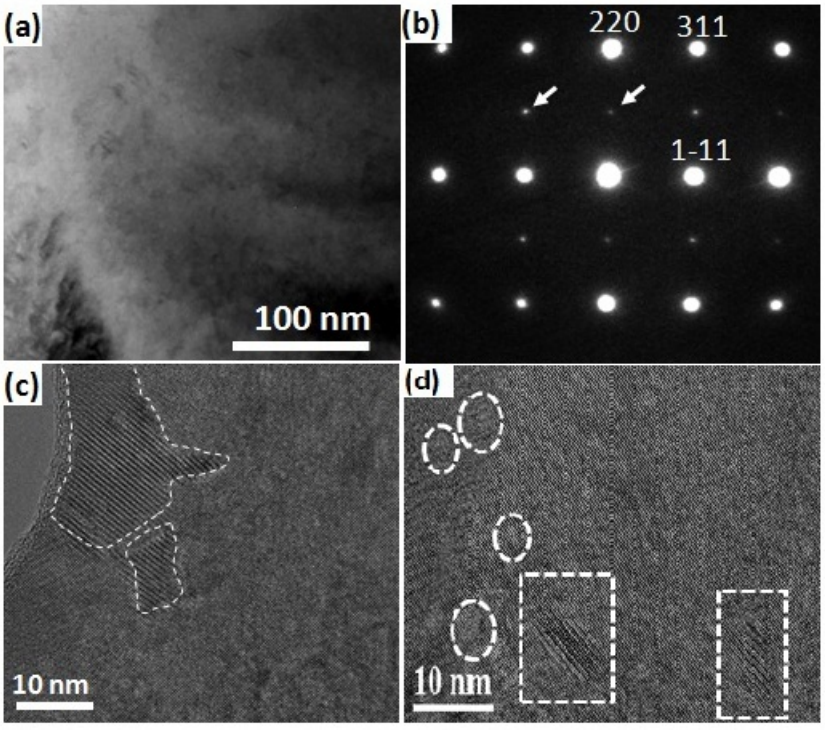

Figure 6.3: Nanoscale architecture of $AgSbSe_2$. (a) Low magnification TEM image of $AgSbSe_2$. (b) Fast Fourier transform (FFT) pattern of (a). Arrows in (b) show the weak superstructure spots. (c, d) High resolution TEM images of $AgSbSe_2$, dotted portion showing nanoprecipitates with the doubling of lattice parameter compared to matrix.

In order to investigate the nanoscale architectures, we have performed transmission electron microscopic (TEM) investigation on pristine $AgSbSe_2$ (Figure 6.3(a)). Although earlier powder X-ray diffraction measurements of $AgSbSe_2$ indicated that Ag and Sb position were disordered in the cation site of the NaCl-type structure[92], careful TEM studies revealed the evidence of local Ag/Sb ordering in nanoscale regions distributed throughout the $AgSbSe_2$ sample. We have also observed weak superstructure spots in the electron diffraction along the $< 110 >$ and $< 201 >$ direction (arrows in Figure 6.3(b)), which resulted due to ordering of Ag and Sb atoms in $AgSbSe_2$. Figure 6.3(c) and Figure 6.3(d) depict representative high resolution TEM (HRTEM) images of $AgSbSe_2$ at two different locations of the sample. Close inspection of the images reveal the presence of two types

of region in the sample. The dotted marked region in the image are nanodomains with doubled lattice parameter (Figure 6.3(c)), which might have formed due to local cation ordering in the $AgSbSe_2$. Similar ordering of cations in $AgSbTe_2$ had been earlier predicted by first-principle calculations for ground state structure [105, 106] and were recently observed by inelastic neutron scattering and TEM investigations in $AgSbTe_2$ [107]. Recent electrical transport measurements on cubic $AgBiS_2$ nanocrystals also indicated the presence of cation ordering near room temperature[84]. The local cation ordering in the nanoscale regime might alter the structure making it non-centrosymmetric locally, which in turn could be responsible for the observed local ferroelectricity in $AgSbSe_2$.

It was suggested in the past that ferroelectric domain-walls might scatter phonons causing a reduction of k_{lat} and enhancement of zT[108]. The effect of ferroelectric domains on the thermoelectric properties may be further investigated by artificially designing the domain structures by nanostructuring and/or by fabricating epitaxial thin films on different substrates[109].

In conclusion, we have performed piezoresponse force microscopy on $AgSbSe_2$ and observed the signature of strong local ferroelectricity and piezoelectricity. From nanoscale structural analysis we show that natural formation of superstructure nanodomains in the sample makes the local crystal structure to be non-centrosymmetric, thereby inducing ferroelectricity. The local dipole could also be created due to the local structural distortion caused by Sb $5s^2$ lone pair. Nano-meter scale ferroelectric domains were clearly imaged by PFM. The naturally occurring ferroelectric domain-walls might act as effective scatterers for phonons and reduce the thermal conductivity of the materials. Our results suggest that ferroelectricity may favour enhanced thermoelectric properties. Therefore, enhancing thermoelectricity by ferroelectric domain engineering might emerge as a promising field of research. Further, it would be interesting to search for ferroelectricity in other known $I-V-VI_2$ thermoelectric semiconductors.

Eight new oligomeric mesogens are reported consisting of an azobenzene-based core attached to which are four 4-cyanobiphenyl units via flexible alkyl spacers (n = 5-12). The oligomers containing n = 8 and n = 10 were found to exhibit a monotropic nematic (N) phase while others were non-mesomorphic. Monolayer film properties of the nematic compound (n = 10) were studied at air-water interface (Langmuir monolayer) and air-solid interface (Langmuir-Blodgett film or LB film). We have carried out atomic force microscope (AFM) studies on LB films transferred onto freshly cleaved hydrophilic mica substrates. The AFM

images in the less density areas showed domains of height of about 2 nm, which corresponds to the estimated height of the molecule showing the formation of monomolecular film. Temperature dependent AFM topography was carried out with the film that showed the reversible formation of aligned fibers (20-40 nm) in the mesophase.

The film was transferred onto hydrophilic and hydrophobic solid substrates by vertical LB technique and the wetting behavior was studied using atomic force microscopy (AFM). Our analysis showed that the film transferred onto a hydrophobic silicon substrate dewets to yield nanodroplets associated with mechanism of spinodal dewetting. Temperature dependent AFM topography indicated that the film showed the reversible formation of aligned fibers in the mesophase. Identification of the temperature dependent structural morphology leading to the formation of aligned microstructures is not only fundamentally significant, but also practically important because it enables rational design and controlling the anisotropic properties of the ordered phase for various applications.

Topography image of the LB film transferred onto a hydrophilic mica substrate at a surface pressure of 35 mN/m is shown in Figure 7.1. In less dense areas the topography showed a uniform film with a height of about 2.1 nm.

In high density areas (Figure 7.2) the film shows network of thin fibres varying between 10 nm to 80 nm. Interestingly, the AFM topography of the films showed the formation of nanodroplets (Figure 7.3(a) and 7.3(b)). The height of the nanodroplets varied between 20-80 nm and did not correspond to the bilayer thickness.

As the most intriguing properties of LC materials are exhibited at mesophase, we thought that it would be worth to look the film topography as a function of temperature.Figure 7.3(c) shows the AFM images of the LB films (shown in 7.3(a) and 7.3(b)) at $114\,^{\circ}\mathrm{C}$. This was achieved by heating the film to the isotropic temperature ($126\,^{\circ}\mathrm{C}$) followed by cooling it to the mesophase temperature. Very interestingly, we observed well-defined aligned fibers (in the same direction) of 20-60 nm at $114\,^{\circ}\mathrm{C}$ under AFM. The film was cooled back to room temperature that showed again the formation of small droplets as was seen earlier prior to heating the sample in the film. This result demonstrated that LC mesophase play an important role into the formation of aligned fibers. This result suggested the reversible transformation of the droplets to fibers and vice versa in the mesophase and at room temperature, respectively.

Appendix A

Comparison with "on"-state data: In Figure 1 we show the spectroscopic data captured in the "on"-state of the pulse applied. In comparison to the "off"-state data (see the main Letter), the overall shape of the "on"-state data is significantly different for all the points. The "on"-state loops are narrower and saturate much faster. The significant difference between the "on"-state and the "off"-state data confirms that the electrostatic effects were minimized in the switching spectroscopy mode.

Topography and phase – before and after domain writing: In Figure 2 we show data complementary to the data presented in Figure 2 and Figure 3 in the main Letter. Here we show that after writing the ferroelectric domains no surface modification was observed indicating that the electrochemical effects were absent. While the phase image before writing did not show any contrast, the circular domain clearly appeared in the phase image captured after writing.

Reproducibility: Temperature evolution of a different domain: In Figure 3 we show the temperature evolution of another circular domain (different from the one presented in the main Letter). We show this here in order to present the reproducibility of the data. This domain was written on a different piece of $SrTiO_3$ crystal.

Time relaxation dynamics: In Figure 4 we show the time evolution of the domain at room temperature. As it is seen, the domain does not completely disappear even after 11 hours indicating that the artificially written domain has a large relaxation time.

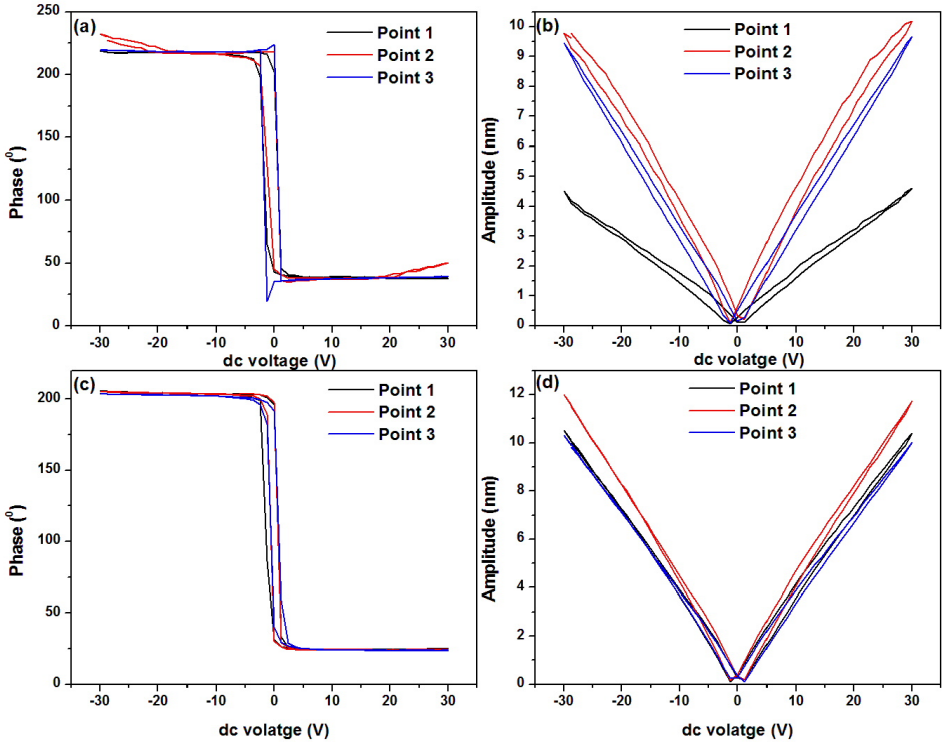

Figure A.1: (a) PFM phase hysteresis and (b) butterfly loops at $300K$ at three different points in the "on" state.(d) PFM phase hysteresis and (e) butterfly loops at $420K$ at three different points in the "on" state.

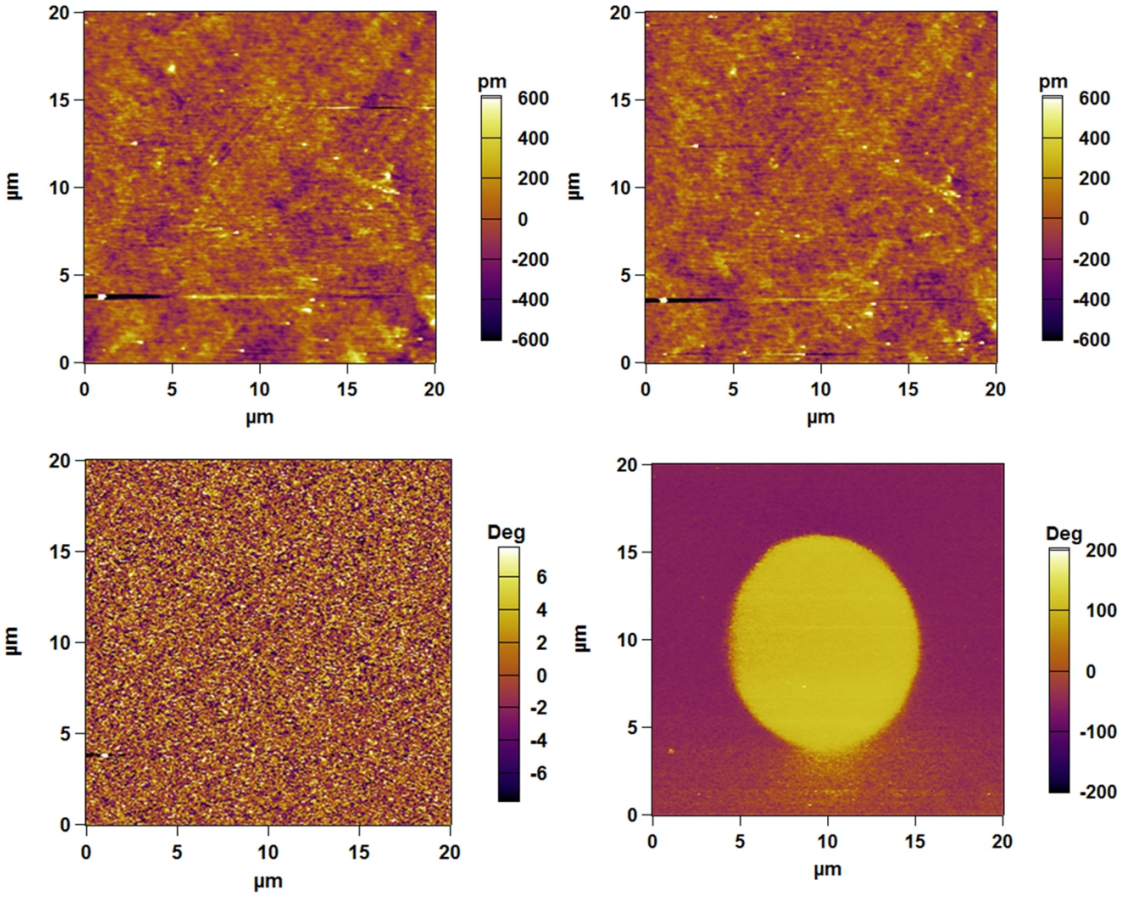

Figure A.2: (a) Topographic and (c)phase image before writing. (b) Topographic and (d) phase image after writing.

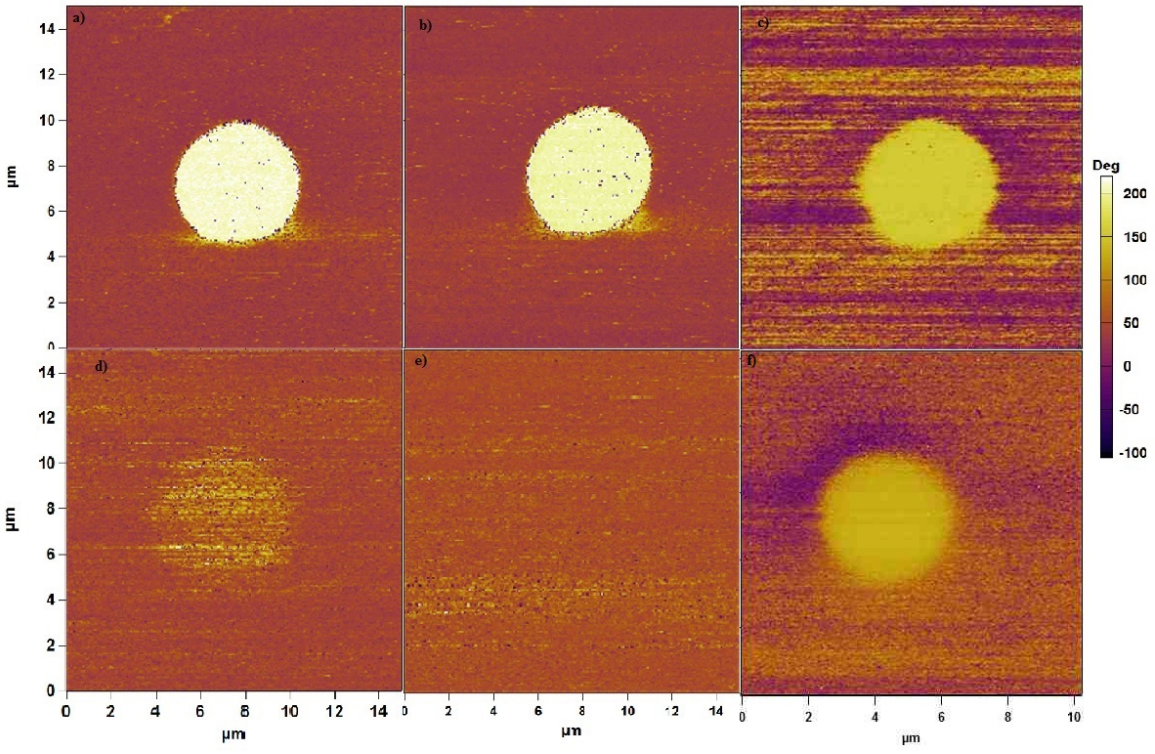

[H]

Figure A.3: (a) A circular domain written on bulk $SrTiO_3$ with $+30V$ on a $14\mu m \times 14\mu m$ area at $300K$. The PFM Phase images of the domain at different temperatures: (b) $320K$ (c) $370K$ (d) $420K$ (e) $440K$; (f) Phase image (at $300K$) of the domain written with $+30V$ at $440K$ and then immediately cooling the sample down to $300K$.

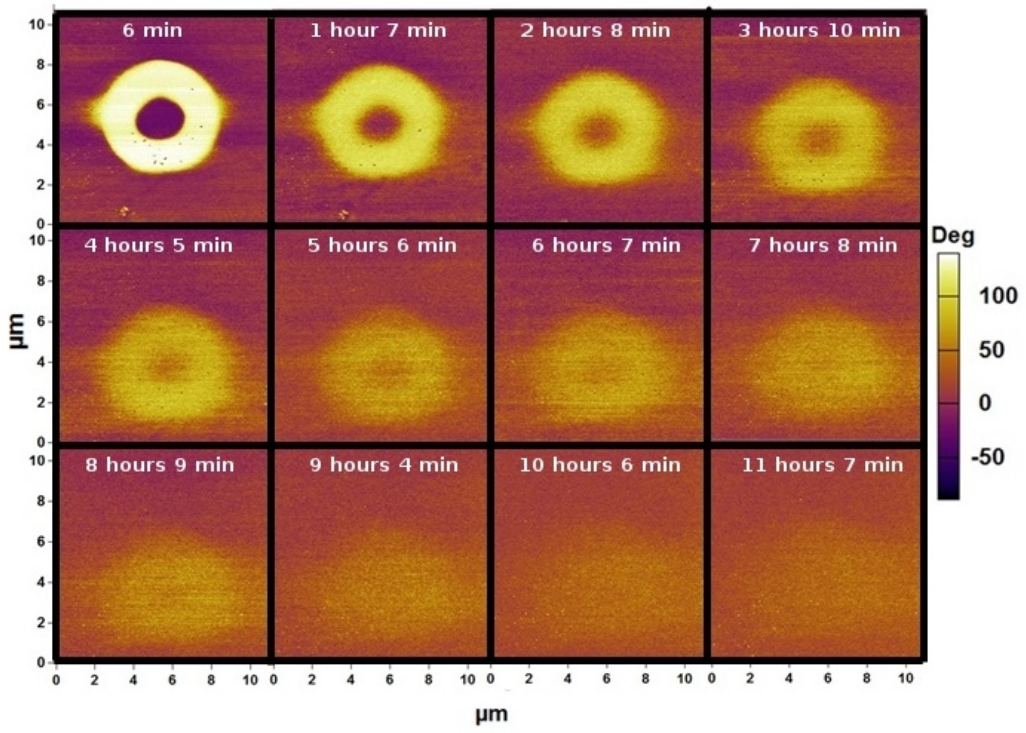

Figure A.4: Phase images showing the time evolution of the domain written at room temperature by applying $+30V$ and erased at center by applying $-30V$.

Bibliography

[1] G. Binnig, H. Rohrer, C. Gerber , E. Weibel “Surface Studies by Scanning tunneling microscopy”. Phys. Rev. Lett. 49,57-61(1982).

[2] G. Binning, C. F. Quate, C. Gerber, “Atomic Force Microscope” Phys. Rev. Lett. 56,930-934(1986).

[3] Lawrence A. Bottomley, “Scanning Probe Microscopy”, Anal. Chem. 70, 425R-475R,(1998).

[4] Guntherodt, H.-J., and R. Wiesendanger, 1991, Eds., “Scanning Tunneling Microscopy” IIII (Springer, Berlin).

[5] I. Giaever, “Energy gap in superconductors measured by electron tunneling”,Phy. Rev. Lett.,5,147-148(1960).

[6] Kuk, Y., and P. J. Silverman, 1988, “Scanning tunneling microscope instrumentation Rev. Sci. Instrum. 60, 165180.

[7] Chen, C. J., 1993, Introduction to Scanning Tunneling Microscopy (Oxford University Press, New York).

[8] Franz J. Giessibl, “Advances in atomic force microscopy” Review of Modern Physics,75,949-983(2003)

[9] T. R. Albrecht, S. Akamine, T. E. Carver, and C. F. Quate “Microfabrication of cantilever styli for atomic force microscope J. Vac. Sci. Technol. A 1990, 8, 33863396.

[10] O. Wolter, Th. Baer, and J. Greshner “Micromachined silicon sensors for scanning force microscopy J. Vac. Sci. Technol. B 1991, 9, 1353-1357.

[11] Asylum Research Manuals for MFP-3D.

[12] Yves F. Dufrłne J. Bacteriol, “Atomic Force Microscope: A Powerful Tool in Microbiology”,2002, 184(19):5205.

[13] D.A. Scrymgeour and V. Gopalan, Phys. Rev. B 72, 024103 (2005).

[14] S.V. Kalinin, E.A. Eliseev, and A.N. Morozovska, App. Phys. Lett. 88, 232904 (2006).

[15] E.A. Eliseev, Sergei V. Kalinin, S. Jesse, S.L. Bravina, and A.N. Morozovska, J. Appl. Phys. 102, 014109 (2007).

[16] B.J. Rodriguez, C. Callahan, S.V. Kalinin, R. Proksch, “Dual-frequency resonance-tracking atomic force microscopy”, Nanotechnology 18 (47), 475504 (2007).

[17] Y. Martin, D. A. Abraham, and H. K. Wickramasinghe High-resolution capacitance measurement and potentiometry by force microscopy Appl. Phys. Lett. 1988, 52, 110310005.

[18] James H. Sang ”Drosophila melanogaster: The Fruit Fly”, (2001-06-23).In Eric C. R. Reeve. Encyclopedia of genetics. USA: Fitzroy Dearborn Publishers, I. p. 157

[19] Byun, D. , Hong, J., Saputra, Ko, J.H., Lee, Y.J., Park, H.C., Byun, B.-K., Lukes, J.R., Journal of Bionic Engineering, 6(1),63-70(2009).

[20] G. S. Watson, S. Myhra, B. W. Cribb, and J. A. Watson, Biophysical Journal,94(8),3352-3360(2008).

[21] T.Wagner, C. Neinhuis, andW. Barthlott, ActaZoologica, 77, 213-225(1996).

[22] G.S. Watson, B.W. Cribb, J.A. Watson, ACS Nano, 4,129136(2010).

[23] Gregory S. Watson, J.A. Watson, S. Hu, C.L. Brown, B. Cribb, S. Myhra, International Journal of Nano manufacturing 5(1),112-128(2010)

[24] F. Song, K.W. Xiaoa, K. Baib, Y.L. Baia, Materials Science and Engineering: A 457,254-26(2007)

[25] Z . Vertesy, Z S . Blint, K . Kertsz , J. P Vigneron, V. Lousse & L . P. Bir. Journal of Microscopy, 224, 108110(2006).

[26] Binetti VR, Schiffman JD, Leaffer OD, Spanier JE, Schauer CL. Integrative Biology, 1(4),324-9(2009).

[27] SS Latthe, AB Gurav, CS Maruti, RS Vhatkar. Journal of Surface Engineered Materials and Advanced Technology, 2, 76-94(2012).

[28] Kesong Liu and Lei Jiang., Nano Today,6(2),155-175(2011).

[29] Elena Celia, Thierry Darmanin, Journal of Colloid and Interface Science.402, 118(2013).

[30] Nicolas Verplanck1, Yannick Coffinier12, Vincent Thomy and Rabah Boukherroub Nanoscale Research Letters, 2,577-596(2007).

[31] N. Huebsch, D. J. Mooney, Nature 462,426-432(2009).

[32] M. Liu, Y. Zheng, J. Zhai, L. Jiang, Accounts of Chemical Research 43,368377(2010).

[33] Lee W, Jin MK, Yoo WC, Lee JK.,Langmuir, 20(18),7665-9(2004).

[34] G.S. Watson and J.A. Watson, Applied Surface Science,235(1), 139144(2004).

[35] Gregory S. Watson, Bronwen W. Cribb, and Jolanta A. Watson. ISRN Biophysics,2012, Article ID 947872(2012)

[36] H. Rumpf, Particle Technology, Chapman and Hall, London, 1990

[37] H.-J. Butt, B. Cappella, M. Kappl, Surface Science Reports 59,1152(2005).

[38] Pittendrigh Barry R.; Raman, Arvind; and Wagner, Ryan, Applied Surface Science,259,225230(2012).

[39] Hsuan-Ming Hu, Jolanta A. Watson, Bronwen W. Cribb and Gregory S. Watson, Biofouling, 27(10), Page 1125 (2011).

[40] Cong Q, Chen G, Fang Y, Ren L. Journal of Bionic Engineering,1, 249255(2004) .

[41] Marden JH, Kramer MG . Science 266,427-430(1994).

[42] G.S. Watson, Bronwen W. Cribb, Jolanta A. Watson. PLoS One,6(9), e24368(2011).

[43] W. Barthlott, C. Neinhuis, Planta 202,18(1997).

[44] Feng L, Li S, Li Y, Li H, Zhang L, Zhai J, Song Y, Liu B, Jiang L, Zhu, D.. Advanced Materials, 14, 1857-1860(2002).

[45] http://arxiv.org/abs/1305.2097, Pramod Kumar, Danish Shamoon, Dhirendra P. Singh, Sudip Mandal, Kamal P. Singh

[46] M. Dawber, C. Lichtensteiger, M. Cantoni, M. Veithen, P. Ghosez, K. Johnston, K. M. Rabe, J.-M. Triscone, Phys. Rev. Lett. **95,** 177601 (2005).

[47] A. Ohtomo, H. Y. Hwang, Nature **427,** 423 (2004).

[48] C. H. Ahn, K. M. Rabe, J.-M. Triscone, Science **303,** 488 (2004).

[49] D. D. Fong, G. B. Stephenson, S. K. Streiffer, J. A. Eastman, O. Auciello, P. H. Fuoss, C. Thompson, Science **304,** 1650 (2004).

[50] M.M. Mehta, D.A. Dikin, C.W. Bark, S. Ryu, C.M. Folkman, C.B. Eom , V. Chandrasekhar, Nature Communications. **3**, 955 (2012).

[51] L. Rimai and G.deMars,Phys.Rev. **127**, 702 (1962).

[52] R.O. Bell and G.Rupprecht, Phys.Rev. **125**,1915 (1962).

[53] W. Zhong, D. Vanderbilt, Phys. Rev. B. **53,** 5047 (1996).

[54] A. Antons, J. B. Neaton, Karin M. Rabe, David Vanderbilt, Phys. Rev. B. **71,** 024102 (2005).

[55] K. A. Müller and H. Burkard, Phys. Rev. B **19**, 3593 (1979)

[56] M. Itoh, R. Wang, Y. Inaguma, T. Yamaguchi, Y-J. Shan, T. Nakamura, Phys. Rev. Lett. **82,** 3540 (1999).

[57] J. H. Haeni, P. Irvin, W. Chang, R. Uecker, P. Reiche, Y. L. Li, S. Choudhury, W. Tian, M. E. Hawley, B. Craigo, A. K. Tagantsev, X. Q. Pan, S. K. Streiffer, L. Q. Chen, S. W. Kirchoefer, J. Levy, D. G. Schlom, Nature **430,** 758 (2004).

[58] O. Bilani-Zeneli, A. D. Rata, A. Herklotz, O. Mieth, L. M. Eng, L. Schultz, M. D. Biegalski, H. M. Christen, K. Dorr, Appl. Phys. Lett. **104,** 054108 (2008).

[59] Y. S. kim, D. J. Kim, T. H. Kim, T. W. Noh, J. S. Choi, B. H. Park, J. G. Yoon, Appl. Phys. Lett. **91,** 042908 (2007).

[60] W. J. Maeng, I. Jung, J. Y. Son, Solid state communications **152,** 1256 (2012).

[61] H.W. Jang, A. Kumar, S. Denev, M.D. Biegalski, P. Maksymovych, C.W. Bark, C.T. Nelson, C.M. Folkman, S.H. Baek, N. Balke, C.M. Brooks, D.A. Tenne, D.G. Schlom, L.Q. Chen, X.Q. Pan, S.V. Kalinin, V. Gopalan, C.B. Eom, Phys. Rev. Lett. **104,** 197601 (2010).

[62] V. Ravikumar, D. Wolf, V. P. Dravid, Phys. Rev. Lett. **74,** 960 (1995).

[63] N. Bickel, G. Schmidt, K. Heinz, K. Muller, Phys. Rev. Lett. **62,** 2009 (1989).

[64] R. Herger, P. R. Willmott, O. Bunk, C. M. Schleputz, B. D. Patterson, Phys. Rev. Lett. **98,** 076102 (2007).

[65] J. S. Sekhon, L. Aggarwal, G. Sheet, e-print arXiv: 1401.2512v1.

[66] R. Proksch, e-print arXiv:1312.6933v1.

[67] S. Jesse, B. Mirman, S. V. Kalinin, Appl. Phys. Lett. **89,** 022906 (2006).

[68] S. Jesse, A. P. Baddorf, S. V. Kalinin, Appl. Phys. Lett. **88,** 062908 (2006).

[69] Yanwu Xie, Christopher Bell, Takeaki Yajima, Yasuyuki Hikita, Harold Y. Hwang, Nano Lett. **10,** 2588 (2010).

[70] C. W. Bark, P. Sharma, Y. Wang, S. H. Baek, S. Lee, S. Ryu, C. M. Folkman, T. R. Paudel, A. Kumar, S. V. Kalinin, A. Sokolov, E. Y. Tsymbal, M. S. Rzchowski, A. Gruverman, C. B. Eom, Nano Lett. **12,** 1765 (2012).

[71] Mengchen Huang, Feng Bi, Chung-Wung Bark, Sangwoo Ryu, Kwang-Hwan Cho, Chang-Beom Eom, Jeremy Levy, e-print arXiv:1208.2687.

[72] N. A. Pertsev, A. K. Tagantsev and N. Setter, Phys. Rev. B **61**, R825 (2000).

[73] Sootsman, J., Chung, D. Y. & Kanatzidis, M. G. New and Old Concepts in Thermoelectric Materials. *Angew. Chem. Int. Ed*. **48,** 8616-8639 (2009).

[74] Snyder, G. J. & Toberer, E. S. Complex thermoelectric materials. *Nature Material* **7,** 105-114 (2008).

[75] Chen, G., Dresselhaus, M. S., Dresselhaus, G., Fleurial, J. P. & Caillat, T. Recent developments in thermoelectric materials. *Int. Mater. Rev.* **48,** 45-66 (2003).

[76] Li, J. F., Liu, W. S., Zhao, L. D. & Zhou, M. High-performance nanostructured thermoelectric materials. *NPG Asia Mater.* **2,** 152-158 (2010).

[77] Tritt, T. M. Thermoelectric phenomena, materials, and applications. *Annu. Rev. Mater. Res.* **41,** 433-448 (2011).

[78] Nielsch, K., Bachmann, J., Kimling, J. & Bottner, H. *Adv. Energy Mater.* Thermoelectric Nanostructures: From Physical Model Systems towards Nanograined Composites. **1,** 713-731 (2011).

[79] Biswas, K. *et al.* Strained endotaxial nanostructures with high thermoelectric figure of merit. *Nat. Chem.* **3,** 160-164 (2011).

[80] Pei, Y. *et al.* Convergence of electronic bands for high performance bulk thermoelectrics. *Nature* **473,** 66-69 (2011).

[81] Heremans, J. P. *et al.* Enhancement of Thermoelectric Efficiency in PbTe by Distortion of the Electronic Density of States. *Science* **321,** 554-557 (2008).

[82] Poudel, B. *et al.* High-Thermoelectric Performance of Nanostructured Bismuth Antimony Telluride Bulk Alloys. *Science* **320,** 634-638 (2008).

[83] Zhao, L. D. *et al.* High thermoelectric performance via hierarchical compositionally alloyed nanostructures. *J. Am. Chem. Soc.* **135,** 7364-7370 (2013).

[84] Guin, S. N. & Biswas, K. Cation Disorder and Bond Anharmonicity Optimize the Thermoelectric Properties in Kinetically Stabilized Rocksalt $AgBiS_2$ Nanocrystals. *Chem. Mater.* **25,** 3225-3231 (2013).

[85] Biswas, K. *et al.* High-performance bulk thermoelectrics with all-scale hierarchical architectures. *Nature* **489,** 414-418 (2012).

[86] Shen, Y., Clarke, D. R. & Fuierer, P. A. Anisotropic thermal conductivity of the Aurivillus phase, bismuth titanate, (Bi4Ti3O12): A natural nanostructured superlattice. *Appl. Phys. Lett.* **93,** 102907:(1-3) (2008).

[87] Lee, S., Bock, J. A., McKinstry, S. T. & Randall, C. A. Ferroelectric-thermoelectricity and Mott transition of ferroelectric oxides with high electronic conductivity. *Journal of the European Ceramic Society* **32,** 3971-3988 (2012).

[88] Bozin, E. S. *et al.* Entropically Stabilized Local Dipole Formation in Lead Chalcogenides. *Science* **330,** 1660-1663 (2010).

[89] Delaire, O. *et al.* Giant anharmonic phonon scattering in PbTe. *Nature Mater.* **10,** 614-619 (2011).

[90] Kolodiazhnyi, T. Insulator-metal transition and anomalous sign reversal of the dominant charge carriers in perovskite $BaTiO_{3-\delta}$. *Phys Rev B* **78**, 045107:(1-5) (2008).

[91] Balke, N. *et al.* Enhanced electric conductivity at ferroelectric vortex cores in $BiFeO_3$. *Nature Physics* **8,** 81-88, (2012).

[92] Guin, S. N., Chatterjee, A., Negi, D. S., Datta, R. & Biswas, K. High thermoelectric performance in tellurium free p-type $AgSbSe_2$. *Energy Environ. Sci.* **6,** 2603-2608 (2013).

[93] Guin, S. N., Negi, D. S., Datta & Biswas, K. Nanostructuring, carrier engineering and bond anharmonicity synergistically boost the thermoelectric performance of p-type $AgSbSe_2 - ZnSe$. *J. Mater. Chem. A.*. **2,** 4324-4331 (2014).

[94] Morelli, D. T., Jovovic, V. & Heremans, J. P. Intrinsically Minimal Thermal Conductivity in Cubic $I - V - VI_2$ Semiconductors. *Phys Rev. Lett.* **101,** 035901:(1-4) (2008).

[95] Nielsen, M. D., Ozolins, V. & Heremans, J. P. Lone pair electrons minimize lattice thermal conductivity. *Energy Environ. Sci.* **6,** 570-578 (2013).

[96] Sekhon, J. S., Aggarwal, L. & Sheet, G. Observation of hysteretic phase switching in silicon by piezoresponse force microscopy. e-print arXiv:1401.2512.

[97] Jesse, S., Mirman, B. & Kalinin, S. V. Resonance enhancement in piezoresponse force microscopy: Mapping electromechanical activity, contact stiffness, and Q factor. *Appl. Phys. Lett*. **89,** 022906:(1-3) (2006).

[98] Jesse, S., Baddorf, A. P. & Kalinin, S. V. Switching spectroscopy piezoresponse force microscopy of ferroelectric materials. *Appl. Phys. Lett*. **88**, 062908:(1-3) (2006).

[99] Please see the supplemental material.

[100] Rodriguez, B. J., Callahan, C., Kalinin, S. V. & Proksch, R. Dual-frequency resonance-tracking atomic force microscopy. *Nanotechnology* **18,** 475504:(1-6) (2007).

[101] Seshadri, R. & Hill, N. A. Visualizing the Role of Bi 6s Lone Pairs in the Off-Center Distortion in Ferromagnetic $BiMnO_3$. *Chem. Mater.* **13,** 2892-2899 (2001).

[102] Waghmare, U. V., Spaldin, N. A., Kandpal, H. C. & Seshadri, R. First-principles indicators of metallicity and cation off-centricity in the IV-VI rocksalt chalcogenides of divalent Ge, Sn, and Pb. *Phys. Rev. B* **67,** 125111:(1-10) (2003).

[103] Neaton, J. B., Ederer, C., Waghmare, U. V., Spaldin, N. A. & Rabe, K. M. First-principles study of spontaneous polarization in multiferroic $BiFeO_3$. *Phys. Rev. B* **71,** 014113:(1-8) (2005).

[104] Rao, C. N. R. & Serrao, C. R. New routes to multiferroics. *J. Mater. Chem.* **17,** 4931-4938 (2007).

[105] Hoang, K., Mahanti, S. D., Salvador, J. R. & Kanatzidis, M. G. Atomic Ordering and Gap Formation in Ag-Sb-Based Ternary Chalcogenides. *Phys. Rev. Lett.* **99,** 156403:(1-4) (2007).

[106] Barabash, S. V., Ozolins, V. & Wolverton, C. First- Principles Theory of Competing Order Types, Phase Separation, and Phonon Spectra in Thermoelectric $AgPb_mSbTe_{m+2}$ Alloys. *Phys. Rev. Lett.* **101,** 155704:(1-4) (2008).

[107] Ma, J. *et al.* Glass-like phonon scattering from a spontaneous nanostructure in $AgSbTe_2$. *Nature Nanotech.* **8,** 445-451 (2013).

[108] Weilert, M. A., Msall, M. E., Wolfe, J. P. & Anderson, A. C. Mode dependent scattering of phonons by domain walls in ferroelectric KDP. *Z. Phys. B* **91,** 179-188 (1993).

[109] Jang, H. w. *et al.* Domain Engineering for Enhanced Ferroelectric Properties of Epitaxial (001) BiFeO Thin Films. *Advanced Mater.* **21,** 817-823 (2009).